Title

Hurricane Irene Sensitivity to Ahead-of-Eye Coastal Ocean Cooling using WRF

Authors

Greg Seroka[1], Travis Miles[1], Yi Xu[2], Josh Kohut[1], Oscar Schofield[1], Scott Glenn[1]

[1]Center for Ocean Observing Leadership, Department of Marine and Coastal Sciences, School of Environmental and Biological Sciences, Rutgers University, New Brunswick, NJ 08901 USA

[2]State Key Laboratory of Estuarine and Coastal Research, East China Normal University, 3663 Zhongshan Road North, Shanghai 200062, China

Corresponding Author: G.S. Seroka, Center for Ocean Observing Leadership, Department of Marine and Coastal Sciences, School of Environmental and Biological Sciences, Rutgers University, New Brunswick, NJ 08901 USA (seroka@marine.rutgers.edu)

Abstract

“Cold wakes” left behind by tropical cyclones (TCs) have been documented since the 1940s. Many questions, however, remain today regarding the specific TC atmosphere-ocean processes that create these cold wakes and their quantified feedback onto storm intensity, due to a paucity of measurements over and within the upper ocean, especially during stormy conditions. Further, the bulk of TC research efforts have investigated deep ocean processes—over which TCs spend the vast majority of their lifetimes—and very little attention has been paid to coastal/shallow water processes. Using Hurricane Irene (2011) as a case study, we quantify the impact of coastal/shallow water SST cooling on storm intensity and structure. We show that significant ahead-of-eye cooling of the coastal ocean (at least 5°C and up to 11°C) occurred during Irene and that this cooling was not captured by basic satellite SST products and coupled ocean-atmosphere hurricane models. We test the sensitivity of Irene’s intensity to the ahead-of-eye cooling and find that it is largest among all tested WRF parameters, while showing that including the cooling in modeling mitigated the high bias in the model predictions. Finally, we provide evidence that this SST cooling—not track, wind shear, or dry air intrusion—was the key missing contribution to Irene’s decay just prior to New Jersey landfall. Rapid and significant intensity changes just before landfall can have substantial implications on storm impacts—wind damage, storm surge and inland flooding— and thus, important coastal ocean processes like ahead-of-eye cooling must be resolved in future hurricane models.

1. Introduction

While tropical cyclone (TC) track prediction has steadily improved over the past two decades, TC intensity prediction has failed to progress in a similarly substantial way (Cangialosi and Franklin 2013). Many environmental factors control TC intensity, including but not limited to the storm track itself, wind shear, intrusion of dry air, potential intensity, and upper-ocean thermal evolution (Emanuel et al. 2004). The last factor, which immediately influences sea surface temperature (SST) evolution and feedback to storm intensity, underlies all other processes, because it directly impacts the fundamental transfer of energy from the ocean to the atmosphere within the TC heat engine (Emanuel 1999; Schade and Emanuel 1999).

Overall, hurricane models today reasonably handle track and large-scale atmospheric processes that affect intensity—wind shear, dry air intrusion, and interaction with midlatitude troughs. Some possible reasons include (i) models' recent considerable improvement in predicting tracks, (ii) the atmosphere receives more attention in modeling, and (iii) models resolve large-scale processes fairly well. However, models do a comparatively poor job of representing oceanic processes that also govern hurricane intensity because they have received relatively little attention and are data limited (Emanuel 1999, 2003; Emanuel et al. 2004).

A specific upper-ocean thermal phenomenon that consistently emerges after a TC is a cold pool of water left in the wake of its path, termed a "cold wake." This oceanic phenomenon has been observed behind TCs since at least the 1940s off the coast of Japan (Suda 1943) and since at least the 1950s in the Atlantic, Caribbean, and Gulf of Mexico (Fisher 1958). Mostly observational studies of the cold wake and potential processes causing the phenomenon, such as upwelling and turbulent entrainment of cold water into the warmer mixed layer, continued into the 1960s (e.g. Leipper 1967). Studies in the late 1970s (Chang and Anthes 1979; Sutyrin and

Agrenich 1979) began the use of idealized numerical simulations to investigate the effect of this oceanic cooling on TC intensity, but neglected TC movement. Then, numerical modeling studies in the 1980s (Sutyrin and Khain 1984) and 1990s (Khain and Ginis 1991; Bender et al. 1993) incorporated TC movement and three-dimensional coupled ocean-atmosphere models to further examine the negative SST feedback on storm intensity.

Prior to the 2000s, observations of the upper ocean beneath a TC were uncommon due to the harsh winds, waves, and currents associated with, and intermittent and unpredictable nature of the storms (D'Asaro 2003). These severe conditions hampered progress in determining detailed physical processes leading to the previously observed "cold wake", as well as specific timing and location of the ocean cooling relative to the TC core. In the 2000s, studies began to provide observational (and model) evidence that significant portions of this surface ocean cooling can in fact occur ahead of the hurricane eye (e.g. D'Asaro 2003; Jacob and Shay 2003; Jaimes and Shay 2009), proposing that such cooling could be a critically important control on hurricane intensity.

Even today, the bulk of research efforts have investigated deep ocean processes and their feedback onto TC intensity; indeed, a TC typically spends the vast majority of its lifetime over the deep ocean (at least 1800 m depth). However, rapid and significant changes in intensity just before landfall and often in shallow water can have substantial implications on storm impacts, i.e. wind damage, storm surge, and inland flooding. Therefore, attention must be paid to shallow water/coastal processes as well (Marks et al. 1998), which inherently differ from deep water processes due to the influence of a shallow ocean bottom and coastal wall.

This paper uses a comprehensive set of novel observational data and cutting-edge modeling techniques to fill two gaps delineated above: a) quantification of the effect of ahead-of-eye upper ocean cooling on TC intensity, and b) the impact of coastal/shallow water processes on TC intensity. Overall, these efforts aim to better understand controls on TC intensity and ultimately improve operational TC forecasting and prediction of impacts.

We analyze a recent landfalling storm, Hurricane Irene (2011) using a combination of unique datasets. Hurricane Irene is an ideal case study because in the days leading up to its landfall in New Jersey (NJ), its intensity was over-predicted by hurricane models (i.e. "guidance") and over-forecast by the National Hurricane Center (NHC) (Avila and Cangialosi 2012). The NHC final report on the storm stated that there was a "consistent high bias [in the forecasts] during the U.S. watch/warning period." NHC attributes one factor in this weakening to an "incomplete eyewall replacement cycle" and a resulting broad and diffuse wind field that slowly decayed as the storm moved from the Bahamas to North Carolina (NC)—over a warm ocean and in relatively light wind shear. Irene made landfall in NC as a category 1 hurricane, two categories below expected strength.

One theory as to why Irene unexpectedly weakened between the Bahamas and NC involves both aerosols and ocean cooling (Lynn et al. 2015). Irene crossed a wide band of Sahara dust just north of the West Indies as well as continental aerosols as it approached land. The authors suggest that Irene absorbed the dust and continental aerosols, which, in combination with SST cooling between the Bahamas and NC, led to the storm's rapid demise.

In this paper, we focus primarily on Irene's time *after* its NC landfall (**Figure 1**), *after* it has weakened in intensity presumably due to aerosol interaction and SST cooling in the South Atlantic Bight (SAB). The operational dynamical models that predicted Hurricane Irene's intensity, in particular, did not fully account for the upper coastal ocean process of rapid and major ahead-of-eye cooling that occurred in the Mid Atlantic Bight (MAB) in the last 24 hours before NJ landfall. The SST cooling over the MAB was at least 3-5 times greater than the SST cooling that occurred south of NC (Glenn et al. 2015, **Figure 2, Figure 3I**).

Here we a) explore how a semi-idealized treatment of ahead-of-eye coastal ocean cooling in the MAB would have altered the predictions, b) hypothesize that better treatment would have lowered the high bias in operational predictions, and c) conclude that this ahead-of-eye coastal ocean cooling observed in Irene was the missing contribution—not wind shear, track, or dry air intrusion—to the rapid decay of Irene's intensity *just prior* to NJ landfall.

2. Data and Methods

2.1 Gliders

Teledyne-Webb Slocum gliders are autonomous underwater vehicles (AUVs) that have become useful platforms for monitoring the ocean's response during storm conditions (Glenn et al. 2008; Ruiz et al. 2012; Miles et al. 2013, 2015). Gliders can provide profiles of the water column from the surface to depths of up to 1000 meters. They continuously sample every two seconds, providing a high temporal resolution time series from pre- to post-storm, in contrast to traditional airborne expendable bathythermograph (AXBT) observational approaches which only provide ocean temperature profiles at one time snapshot. Finally, gliders can be piloted, enabling more targeted profiling throughout the storm, in contrast to Argo and ALAMO floats which passively move with the ocean currents. A more detailed description of the gliders and their general capabilities can be found in *Schofield et al. 2007*. For storm-specific capabilities of the gliders, see *Miles et al. 2013, 2015*.

RU16 glider was used in this study. The glider was equipped with several science sensors, including a Seabird un-pumped conductivity temperature and depth (CTD) sensor, which measured temperature, salinity and water depth. Here we only use the top bin in the temperature profiles to provide a measure of near-surface temperature at the glider location (Figure 1).

2.2 Buoys

2.2.1 Near-surface temperature

National Data Buoy Center (NDBC) buoys 41037 and 41036 in the SAB and buoys 44100, 44009, and 44065 in the MAB were used in this study (**Figure 1**). Here, only hourly water temperature was used, which is measured at 0.6 m depth at all buoys except 0.46 m depth at 44100. These data provide an idea of near-surface water temperature evolution along and near the track of Hurricane Irene through the SAB and MAB.

2.2.2 Heat fluxes

NDBC buoys 44009 and 44065 were used for latent and sensible heat flux calculations, which were estimated based on the “bulk formulae” (Fairall et al. 1996):

Sensible heat flux: $H = -(\rho c_p)C_H U(\theta - \theta_{sfc})$ (1)

Latent heat flux: $E = -(\rho L_v)C_Q U(q - q_{sfc})$ (2)

where ρ is density of air, c_p is specific heat capacity of air, C_H is sensible heat coefficient, U is 5m wind speed, θ is potential temperature of the air at 4m and θ_{sfc} is potential temperature at the water surface, L_v is enthalpy of vaporization, C_Q is latent heat coefficient, q is specific humidity of the air at 4m, and q_{sfc} is interfacial specific humidity at the water surface.

θ_{sfc} and q_{sfc} are both not directly computed from interfacial water temperature, but rather computed from temperature measured at 0.6m depth at the buoy. During high wind conditions, the difference between skin temperature and temperature at 0.6m depth is likely small enough to have a negligible effect on the computed bulk fluxes (Fairall et al. 1996). Finally, RH measurements at 4m from the buoys may have larger uncertainty during Irene's high wind conditions due to sea spray; this uncertainty has not been quantified for this study.

2.3 Satellites

2.3.1 SST

To attain a new cloud-free, coldest dark-pixel SST composite, we:

1. Clean up Advanced Very High Resolution Radiometer (AVHRR) daytime-only (12-20 UTC) scans from NOAA-18 and NOAA-19 satellites
    a. AVHRR Channel 2 needs daylight because it is near visible
2. Remove cloudy pixels in each scan, specific to MAB:
    a. AVHRR Channel 2 (0.725-1 μm) tests:
        i. Remove if near IR albedo > 2.3%
        ii. Remove if Δnear IR albedo > 0.15% within ~3km x 3km box
    b. AVHRR Channel 4 (10.3-11.3 μm) tests:
        i. Remove if T < 5°C (summer), 3.5°C (winter)
        ii. Remove if ΔT > 1°C within ~3km x 3km box
3. Create 3-day "coldest pixel composite" of 12-20 UTC AVHRR "declouded" scans with NASA Short-term Prediction Research and Transition (SPoRT) 2km SSTs

The thresholds used in the AVHRR channel tests to remove cloudy pixels were established through a series of diagnostic tests to determine optimal performance specifically for the MAB. We perform a coldest pixel composite of the resulting "declouded" AVHRR scans to preserve any ocean cooling processes that may occur, including TC cooling and coastal upwelling. In contrast, warmest pixel compositing is commonly used in global Multi-Channel

SST (MCSST) algorithms to remove any cloudy pixels, which would also result in eliminating any TC cooling.

The National Centers for Environmental Prediction (NCEP) Real-Time Global High-Resolution (RTG-HR) is a daily SST analysis that is also used in this study. RTG-HR is operationally produced using in situ and AVHRR data on a 1/12° grid (Reynolds and Chelton 2010). The operational 13km Rapid Refresh (RAP) and the 12km North American Mesoscale model (NAM) and its inner nests, including the 4km NAM CONUS nest, uses fixed-in-time RTG-HR as its SST. Therefore, RTG-HR is a very relevant SST product for cross-comparison with our 2km SST composite described above.

2.3.1 Water vapor

In addition to SST, satellites are used in this study for a spatial estimate of the intrusion of dry air into Irene's circulation. We use Geostationary Operational Environmental Satellite (GOES) 13 Water Vapor Channel 3 brightness temperature imagery for these estimates.

2.4 Radiosondes

Radiosondes, typically borne aloft by a weather balloon released at the ground, directly measure—from the bottom of the troposphere to the stratosphere—temperature, humidity, pressure and derive wind speed and direction among other variables. To validate profiles of modeled wind shear and dry air intrusion, we use radiosonde observations of u and v winds from Buffalo International Airport, NY (KBUF) and relative humidity (RH) from Wallops Island, VA (KWAL).

2.5 North American Regional Reanalysis (NARR)

The North American Regional Reanalysis (NARR) is the last data product we used to evaluate our modeling. NARR is a high-resolution (32-km, 45 vertical layer) reanalysis produced by NCEP and provides a long-term (1979-present) set of consistent atmospheric data on the North American scale. The data consists of reanalyses of the initial state of the atmosphere, which are produced by using a consistent data assimilation scheme to ingest a vast array of observational data into historical model hindcasts. NARR is used to evaluate modeled size and structure of Irene, modeled heat fluxes, and modeled wind shear, both horizontally and vertically.

2.6 Modeling and Experimental Design

2.6.1 Hurricane Weather Research and Forecasting (HWRF)

Output from two different versions of the Hurricane Weather Research and Forecast system (HWRF) was used in this study: 1) the operational HWRF which is the atmospheric Weather Research and Forecast model (WRF) coupled to the feature-model-based Princeton Ocean Model (HWRF-POM), and 2) the same atmospheric WRF component but coupled to the Hybrid Coordinate Ocean Model (HWRF-HYCOM).

For the operational 2011 hurricane season, POM for HWRF-POM was run at 1/6° resolution (~18km), with 23 terrain-following sigma coordinate vertical levels. Three-dimensional output data from POM are interpolated vertically onto the 23 half-sigma vertical levels occurring where ocean depth is 5500 m (Tallapragada et al. 2011). The top level from which we pull near-surface temperature occurs at 5m.

The ocean model component of HWRF-HYCOM is the Real-Time Ocean Forecast System-HYCOM (RTOFS-HYCOM), which varies smoothly in horizontal resolution from ~9km in the Gulf of Mexico to ~34km in the eastern North Atlantic (Kim et al. 2014). We pull data from the top layer of HYCOM for near-surface temperature.

2.6.2 ROMS

The Regional Ocean Modeling System (ROMS, http://www.roms.org, Haidvogel et al. 2008) is a free-surface, sigma coordinate, primitive equation ocean model that has been particularly used for coastal applications. Specifically, we use output from simulations run on the ESPreSSO (Experimental System for Predicting Shelf and Slope Optics) model (Wilkin and Hunter 2013) grid, which covers the MAB from Cape Hatteras to Cape Cod, from the coast to the shelf break and beyond, at 5km horizontal resolution and with 36 vertical levels.

2.6.3 WRF and Experimental Design

The Advanced Research dynamical core of WRF (WRF-ARW, http://www.wrf-model.org, Skamarock et al. 2005), Version 3.4 is a fully compressible, non-hydrostatic, terrain-following vertical coordinate, primitive equation atmospheric model. Our WRF-ARW domain extends from South Florida to Nova Scotia, and from Michigan to Bermuda (Glenn et al. 2015).

In our experiments, the control simulation has a horizontal resolution of 6km with 35 vertical levels. The following physics options are used: longwave and shortwave radiation physics were both computed by the Rapid Radiative Transfer Model-Global (RRTMG) scheme; the Monin-Obukhov atmospheric layer model and the Noah Land Surface Model were used with the Yonsei University planetary boundary layer (PBL) scheme; and the WRF Double-Moment 6-class moisture microphysics scheme was used for grid-scale precipitation processes.

It was critical to ensure that our control simulation had a track very similar to the NHC best track, so as to not include any land effects on the intensity of Irene, which tracked closely along the coast. Several different lateral boundary conditions and initialization times were experimented with before arriving at the best solution. The resulting lateral boundary conditions used are from the Global Forecast System (GFS) 0.5° operational cycle initialized at 06 UTC on 27 August 2011.

For the control simulation, we use RTG HR SST from 00 UTC 27 August 2011 for bottom boundary conditions over the ocean. This is six hours prior to model initialization, to mimic NAM and RAP operational conditions. All simulations, including the control, are initialized at 06 UTC on 27 August 2011 when Irene was just south of NC and end at 18 UTC on 28 August 2011 (**Figure 1**). By initializing so late, we focus only on changes in Irene's intensity occurring in the MAB, after any changes that could have occurred farther south in the SAB.

To answer the question, *why did model guidance not fully capture the rapid decay of Irene just prior to NJ landfall?* we conduct a two-part experiment:

Part 1) 130 sensitivity tests of Irene's intensity, size, and structure to various model parameters, physics schemes, and options, including horizontal and vertical resolution, microphysics, planetary boundary layer (PBL) scheme, cumulus parameterization, longwave and shortwave radiation, land surface physics, air-sea flux parameterizations, 1D ocean mixed layer (OML) model, and SST, and

Part 2) validation/evaluation of the control run's treatment of track, wind shear, and dry air intrusion, the three other—outside of upper ocean thermal evolution—major governing factors of TC intensity.

Part 1 allows us to quantify the sensitivity of Irene's modeled intensity, size, and structure to SST, and put that sensitivity into context by comparing it to other model parameter sensitivities. Part 2 allows us to complete the test of our hypothesis that the other major governing factors of TC intensity were sufficiently handled by the control simulation and that upper ocean thermal evolution in the MAB was therefore the missing contribution to Irene's demise just prior to NJ landfall.

To conclude the experimental design section, details on a few key sensitivities performed in Part 1 are provided. These are: SST, air-sea flux parameterizations, 1D OML model, and latent heat flux <0 over water.

2.6.3.1 Sensitivity to SST

To show the maximum impact of the "ahead-of-eye" SST cooling on storm intensity, we compared our control run using a static warm pre-storm SST (RTG HR SST) to a simulation using observed cold post-storm SSTs. For this cold SST, we used our cloud-free, coldest dark-pixel SST composite (described in section 2.2.1) from 31 August 2011 (**Figure 3E**). According to underwater glider and NDBC buoy observations along Irene's entire MAB track (**Figure 1**), almost all of the SST cooling in the MAB occurred ahead of Irene's eye (**Figure 2C-F**). The SAB also experienced ahead-of-eye SST cooling, but values are on the order of 1°C or less (**Figure 2A-B**). Because our model simulations include only 6 hours of storm presence over the SAB before NC landfall, and SST cooling in the SAB was significantly less than observed in the MAB, we can conclude that the main result from our SST sensitivity is due to the ahead-of-eye cooling only in the MAB.[1]

2.6.3.2 Sensitivity to air-sea flux parameterizations

In section 2.2.2, we listed the bulk formulae for sensible and latent heat fluxes. The following is the equation for momentum flux:

Momentum flux: $$\tau = -\rho C_D U^2 \quad (3)$$

where ρ is density of air, C_D is drag coefficient, and U is 10 m wind speed.

[1] It will be shown in the results that this semi-idealized treatment of ahead-of-eye cooling in the model—using cold post-storm SST—is actually not an overestimate in the impact of cooling on Irene's intensity, but rather an underestimate when validating modeled air-sea heat fluxes against in situ fluxes.

Three options exist in WRF-ARW Version 3.0 and later for air-sea flux parameterizations (WRF namelist option isftcflx=0, 1, and 2; see Green and Zhang 2013 for more details). These parameterization options change the momentum (z_0), sensible heat (z_T), and latent heat roughness lengths (z_Q) in the following equations for drag, sensible heat, and latent heat coefficients:

Drag coefficient: $C_D = k^2/[\ln(z_{ref}/z_0)]^2$ (4)

Sensible heat coefficient: $C_H = (C_D^{1/2})[k/\ln(z_{ref}/z_T)]$ (5)

Latent heat coefficient: $C_Q = (C_D^{1/2})[k/\ln(z_{ref}/z_Q)]$ (6)

where k is the von Kármán constant and z_{ref} is a reference height (usually 10 m).

Therefore, our SST sensitivity effectively changes the variables θ_{sfc} and q_{sfc} in equations 1-3 above, while our air-sea flux parameterization sensitivities change the equations for the momentum, sensible heat, and latent heat coefficients (equations 4-6) going into the respective flux equations (1-3).

For our air-sea flux parameterization sensitivities in this study, we ran isftcflx=0, 1, and 2 with both the warm (control) and cold SST boundary conditions.

2.6.3.3 Sensitivity to 1D ocean mixed layer model

Pollard et al.'s (1972; described in WRF context by Davis et al. 2008) 1D ocean mixed layer model was used to test the sensitivity of Irene to 1D ocean processes. Two different initializations of the 1D ocean model were used: 1) initializing the mixed layer depth (MLD) everywhere to 10m and the slope of the thermocline everywhere to 1.6°C/m according to underwater glider observations in the MAB (Glenn et al. 2015), and 2) initializing the MLD spatially using HYCOM and slope of the thermocline everywhere to 1.6°C/m. However, as will be shown in the results, there were major issues using both options to accurately determine sensitivity to 1D ocean processes.

2.6.3.4 Sensitivity to latent heat flux <0 over water

In the WRF surface layer scheme code, there is a switch that does not allow any latent heat flux less than 0 W m-2. (There is also a switch that disallows any sensible heat flux less than -250 W m-2). WRF convention for negative heat flux is downward, or from the atmosphere to land or water surface. This sensitivity involves removing the switch disallowing negative latent heat flux. This switch removal only results in changes in latent heat flux over water, because the subsequent WRF land surface scheme modifies fluxes and already allows for latent heat flux to be negative over land.

3. Results

3.1 Sensitivity Tests

Motivation

The coastal track of Irene (**Figure 1**) over the highly-populated and highly-instrumented Mid-Atlantic and Northeast U.S. allowed for a truly comprehensive look into the details and timing of coastal ocean cooling, from the SAB to the MAB. All in-water instruments employed in this paper were virtually fixed points in space and within 70 km from Irene's eye, including station-keeping RU16 glider, providing an Eulerian look at the ahead-of-eye SST cooling occurring near the storm's inner core. RU16 glider profiled the entire column of water over the MAB continental shelf, providing a view of the full evolution of upper ocean in response to Irene. The rapid two-layer shear-induced mixing process that led to ahead-of-eye cooling of the coastal ocean is described in detail in Glenn et al. 2015. For the purposes of this paper, we focus on SST response and feedback on Irene's intensity.

The buoys in the SAB (41037 and 41036) documented ~1°C SST cooling in the front half of the storm, ahead of the eye, with total SST cooling less than 2°C (**Figure 2**, eye passage at each buoy indicated by vertical dashed line). In contrast, the MAB buoys (44100, 44009, and 44065), as well as RU16 glider, observed 4-6°C SST cooling ahead-of-eye, with only slight cooling after eye passage of less than 2°C (**Figure 2**). Therefore, the buoys and glider provide detailed evidence that significant ahead-of-eye cooling occurred in the MAB.

While the buoys provided information on the timing of SST cooling, our high-resolution SST composite showed the spatial extent and variability of the cooling, and revealed that the cooling was not captured by basic satellite products and some models used to forecast hurricane intensity. Our improved SST composite showed pre-storm (26 Aug 2011, **Figure 3A)** and post-storm (31 Aug 2011, **Figure 3E)** SST conditions along the U.S. East Coast. SST cooling to the right of storm track in the SAB approached 2°C, and in the MAB approached 11°C at the mouth of the Hudson Canyon (**Figure 3I**). Under the TC inner core, within 25km of Irene's track, SST cooling in the SAB ranged from 0.5 to 1.5°C, while in the MAB cooling ranged from ~2 to ~4°C (**Figure 3M**). It is important to note that the SST composite from three days after storm passage is used for post-storm conditions, because clouds had sufficiently cleared over the MAB by that time. However, analysis of individual AVHRR scans indicated no additional cooling occurred in the MAB—due to processes other than the direct storm forcing, such as inertial mixing—from one day after to three days after storm passage (not shown). Therefore, all cooling shown in Figure 3I occurred ahead of and under the storm's inner core strong wind environment.

RTG HR SST pre- (26 Aug, **Figure 3B**), post-storm (31 Aug, **Figure 3F**), and difference (31 Aug minus 26 Aug, **Figure 3J**) plots show spatially similar cooling patterns to the new high-resolution coldest pixel SST composite, but cooling magnitudes are lower, especially to the right of storm track in both the SAB and MAB (**Figure 3N**). Similarly, there was no significant additional MAB cooling in RTG HR SST from one day after (not shown) to three days after (**Figure 3F**) storm passage.

HWRF-POM (**Figure 3C, G, K, O**) and HWRF-HYCOM (**Figure 3D, H, L, P**) model results are also shown for comparison to coupled ocean-atmosphere hurricane models. Pre-storm (00UTC Aug 26) and post-storm (00UTC Aug 31) times for both model results are coincident with the coldest dark pixel SST composite and RTG HR SST composite times, and both model simulations shown are initialized at 00UTC on 26 Aug. Therefore, the post-storm SST conditions are 5-day forecasts in both models. Again, there are no significant differences in MAB SST cooling between immediately after and three days after Irene's passage in both HWRF-POM and HWRF-HYCOM. Like RTG HR post-storm SST (**Figure 3F**), HWRF-POM (**Figure 3G**) and HWRF-HYCOM (**Figure 3H**) post-storm SST in the MAB are several degrees too warm—coldest SSTs are 20-23°C, where they should be 17-20°C. Therefore, coupled atmosphere-ocean models designed to predict TCs did not fully capture the magnitude of SST cooling that resulted from Hurricane Irene, especially in the MAB. The question is, does this uncaptured cooling have an effect on the intensity of the storm, especially because the eye of the storm was over the MAB for only ~9.5 hours and very near the coast, so only the eastern half of the storm was over water. We answer this question in the next part, and also determine if accounting for this cooling in modeling lowers the high bias in Irene's forecasted intensity.

Sensitivity results

Over 130 WRF simulations were conducted to test the sensitivity of modeled Irene intensity to the observed ahead-of-eye cooling and to various other model parameters. Only those simulations with tracks within 50km of NHC best track were retained, leaving 26 simulations (**Table 1**).

To quantify cumulative model sensitivities, the sum of the absolute value of the hourly difference between the control run minimum SLP (and maximum sustained 10m winds) and experimental run minimum SLP (and max 10m winds) was taken, but only from 23UTC on 27 Aug to the end of the simulation. This confines the sensitivity to the time period of Irene's presence over the MAB and thereafter. The equation is as follows:

$$\sum_{i=23UTC\ 27Aug}^{i=18UTC\ 28Aug} |\min SLP[control(@hour\ i)] - \min SLP[exp.(@hour\ i)]| \qquad (7)$$

Figure 4 shows the results of model sensitivity as measured by minimum SLP (left) and maximum 10m wind speeds (right). Over the 20 hours calculated, the three largest sensitivities when considering both intensity metrics were due to SST (fixed warm pre-storm vs. fixed cold post-storm SST) with the three WRF air-sea flux parameterization options (*isftcflx*=1, 2, 3). On average, for SST over the three options, pressure sensitivity was 66.6 hPa, or 3.33 hPa hr^{-1}, and wind sensitivity was 52.0 m s^{-1}, or 2.6 m s^{-1} hr^{-1}.

As mentioned above, there were major issues with using the 1D OML model to accurately determine sensitivity to 1D ocean processes. The issue with the first option of initializing the MLD to 10m and slope of the thermocline to 1.6°C/m everywhere is that the Gulf Stream is very warm and well mixed down to 100-200m (Fuglister and Worthington 1951). Initializing the Gulf Stream MLD to 10m resulted in cold water only 10m deep that was quickly mixed to the surface and cooled the SSTs. Therefore, the resulting sensitivity to this option (72.7 hPa, 42.4 m s^{-1}) was artificially high, because in reality, the Gulf Stream would not be mixed. The issue with the second option of using HYCOM for the spatial estimate of initial MLD was that HYCOM had problems mixing and cooling the surface waters over the MAB continental shelf, so this sensitivity (21.1 hPa, 22.2 m s^{-1}) is likely too low.

The SST and Advanced Hurricane WRF sensitivities along with the top two remaining sensitivities for each intensity metric are presented in time series in **Figures 5A and 6A**. The black line indicates NHC best track estimates of intensity, while the red lines indicate the three WRF air-sea flux parameterization options using the warm pre-storm SST, the blue lines indicate the same but for the cold post-storm SST, the two cyan lines indicate the two 1D OML model initializations, the magenta line indicates cumulus parameterization, and the green line vertical resolution for min SLP (Figure 5A) and PBL scheme for max winds (Figure 6A). Note that min SLP at initialization is about 975 hPa whereas NHC best track indicates 952 hPa at that time; this difference is due to issues with bogus vortexing within WRF, and it only takes 6 hours for the model to adjust and drop to 953 hPa, only 1 hPa within NHC best track. Sensitivity to digital filter initialization (DFI) to remove ambient noise at initialization was performed, which resulted in initial min SLP to be ~958 hPa, a reduction of 17 hPa (with little impact on initial max winds) (Glenn et al. 2015). However, downstream sensitivity to using DFI was negligible, indicating that for this series of simulations, the seemingly major initialization issue does not seem to have a major effect on downstream intensity.

Figures 5B and 6B show the time evolution of three sensitivities: 1) SST, warm vs. cold (black), 2) air-sea flux parameterization with warm SST, *isftcflx*=0 vs. 1 (red), 3) air-sea flux parameterization with cold SST, *isftcflx*=0 vs. 1 (blue). For both intensity metrics, sensitivity to SST gradually increases from about equal to flux parameterization sensitivity upon entrance to the MAB (first gray vertical dashed line) to almost triple it (~5 hPa vs. ~2 hPa, 6 m s^{-1} vs. ~0-2 m s^{-1}) upon exit out of the MAB (second gray vertical dashed line). Finally, Figures 5C and 6C show box and whisker plots of the simulation error as compared to NHC best track, only during MAB presence (23 UTC 27 Aug to 13 UTC 28 Aug); r squared values are shown at the bottom in bold. The three warm SST simulations have a min SLP too low and max wind speed too high, while the three cold SST simulations have a min SLP closer to NHC best track and a max wind speed slightly lower than NHC best track. Because of the high uncertainty (~4 m/s or higher) associated with NHC best track wind estimates for the North Atlantic Basin, we focus on errors using the pressure metric that has lower uncertainty (3-4 hPa for non-major hurricanes) (Torn and Snyder 2012; Landsea and Franklin 2013). The highest r squared values were found with the three cold SST simulations; while this could partly be due to luck, it is clear that including a more accurate representation of the ahead-of-eye cooling via fixed cold post-storm SSTs (rather than fixed warm pre-storm SST as standard in many operational weather models) lowers the high bias in our model's prediction of intensity.[2]

So far we have only addressed how overall estimates of intensity (min SLP and max winds) change with each sensitivity. How does the size and structure of Irene change? To spatially evaluate WRF results, NARR SLP and winds are used (**Figure 7**). Spatial plots of SLP are shown from NARR (Figure 7A), WRF warm SST (Figure 7B), and WRF cold SST (Figure 7C) runs, at just before NJ landfall. Only slight differences exist between WRF simulations, mainly in Irene's central pressure (warm SST: 955.4 hPa, cold SST: 959.1 hPa); overall size and spatial structure of the storm is very similar between runs. The WRF simulations also compare well in size and shape to NARR SLP, but do not in central pressure (NARR: 975.9 hPa). This is

[2] Further, notice the overall deep bias in modeled min SLP *prior* to storm presence over the MAB (12 UTC Aug 27 to 23 UTC Aug 28). If we somehow alter the simulations so that the entire time series of min SLP was deeper, the warm SST runs would be even deeper over the MAB time period, and the cold SST runs would still be lowering the even deeper deep bias.

likely due to NARR resolution issues, as the NHC best track estimate of central pressure at landfall, only 35 min after, is 959 hPa.

Similar results are shown in spatial plots of 10m winds (**Figure 8**). General size and structure, especially over land, agrees well among NARR, warm SST, and cold SST runs, but major differences exist over the MAB waters. NARR shows a maximum wind speed of 22.7 m s^{-1}, whereas the WRF warm SST (33.0 m s^{-1}) and cold SST (31.0 m s^{-1}) simulations are much closer to NHC best track's estimate of 30.9 m s^{-1}. Besides a general overall reduction in wind speed in the cold SST simulation, little difference is noted in size of Irene between warm and cold SST. This is verified by a radius of max wind comparison between the warm and cold SST simulations and b-deck data from the Automated Tropical Cyclone Forecast (ATCF, Sampson and Schrader 2000) system database (Table 2). The b-deck data, available every 6 hours, shows good agreement with both warm and cold SST simulations, with 7 nmi or less difference between warm and cold SST for the first 24 hours of simulation, and 11 nmi or less difference between model and "observed" b-deck radii. At 12UTC on 28 Aug, the cold SST simulation shows a much larger radius of max winds, likely due to the strongest winds occurring in an outer band thunderstorm and indicating more rapid enlargement of storm size in that simulation.

Vertical east-west (**Figure 9A-C**) and north-south (**Figure 9D-F**) cross sections of wind speeds through the eye of Irene at 09 UTC on 28 Aug, just before landfall, tell the same story—that NARR has issues reproducing the higher wind speeds not only at 10m but through the entire atmosphere, and that there is only slight differences in wind speed structure between the warm and cold SST simulations. Both simulations show an asymmetric storm west to east with the core of the strongest winds over water, on the right side of the eye, extending all the way up to the tropopause at about 200 hPa (**Figure 9B and C**), with the warm SST run showing much higher wind speeds from ~950 hPa to 700 hPa. On the left side of the eye, the strongest winds extend only up to 700-800 hPa and the core is much narrower from west to east. The north-south cross sections show a more symmetric storm, as well as the outer edges of the Jet Stream at about 200 hPa and 45°N.

Because air-sea heat fluxes drive convection, TC circulation and thus resulting TC intensity, a closer look at the sensible and latent heat fluxes is warranted, to determine just how sensitive they are to a change in SST. We plot the fluxes spatially at 06 UTC 28 Aug in **Figure 10**, and temporally at two MAB buoys in **Figure 11**. The largest modeled latent and sensible heat fluxes correlate well spatially with the strongest winds in NARR, warm SST, and cold SST runs (**Figure 10**). However, there are large differences in both latent and sensible heat fluxes between the warm and cold SST runs, most notably over the MAB where a reverse in the sign of both latent and sensible heat fluxes occurs. In some locations over the MAB, the warm SST run shows a few hundred Wm^{-2} in latent heat flux directed from the ocean to the atmosphere (**Figure 10E**), whereas the cold SST run shows several hundred Wm^{-2} in the opposite direction (**Figure 10F**). NARR also shows slightly negative latent heat flux over the MAB (NARR fluxes are 3-hr averages). Similar patterns are evident in sensible heat flux, but at a much smaller magnitude. It is important to note that a negative latent heat flux over water—directed from the atmosphere to the ocean—is disallowed in WRF (similarly, sensible heat fluxes <250 Wm^{-2} are also disallowed over water). What is shown for the cold SST run in Figure 10 is the cold SST simulation from sensitivity number 18 (**Table 1**), with latent heat flux <0 allowed over water. When negative latent heat flux is not allowed, all negative latent heat fluxes (e.g. the blue areas in Figure 10F) become zero (not shown).

The negative latent heat fluxes were also "observed" at both buoys at which they were calculated—44009 and 44065. At both buoys, for almost the entire times shown, air temperature was greater than SST—in some cases over 4.5°C warmer (**Figure 11A, B**). These largest temperature differences occurred either during or right at the end of the SST cooling at each buoy, and coincided with the largest calculated "observed" negative latent heat fluxes—about -200 to -250 Wm^{-2} at both buoys (**Figure 11C, D**). At this time, NARR latent heat fluxes approached -120 Wm^{-2} at 44009 and -40 Wm^{-2} at 44065. The cold SST WRF simulation shows latent heat fluxes zeroed out this whole time period (**Figure 11C, D**), and approaching -180 Wm^{-2} at 44009 and -130 Wm^{-2} at 44065 when negative latent heat fluxes are allowed **(Figure 11E, F**). Meanwhile, the warm SST simulation shows latent heat fluxes with opposite sign, approaching 470 Wm^{-2} toward the end of the simulation at 44009 and 530 Wm^{-2} at 44065. Further, heat flux sensitivity to air-sea flux parameterizations was low, especially when compared to its sensitivity to warm vs. cold SST. This evaluation of air-sea heat fluxes confirms that our cold SST simulation not only begins to resolve the negative latent heat fluxes that have been indicated by observations, but also approaches such negative values that can have a significant impact on storm intensity.

3.2 Validation of Track, Wind Shear, and Dry Air Intrusion

To test our hypothesis that upper ocean thermal structure and evolution in the MAB was the missing contribution to Irene's decay in the final hours prior to NJ landfall, here we evaluate the control run's treatment of track, wind shear, and dry air intrusion.

Track was handled very well by the simulations, remaining within 30 km for the entire time series for the control run and until landfall for the cold SST sensitivity (**Figure 1, Table 3**). As Irene tracked so close to shore, this was critical for teasing out any potential impact from land interactions in subsequent sensitivities.

Wind shear values within and ahead of Irene during its MAB presence were similarly handled well by the simulations. We chose 250-850 hPa as the levels at which to calculate wind shear (instead of the standard 200-850 hPa) because our area of focus is in the mid-latitudes where the tropopause is slightly lower in altitude than over the tropics. At the time of entrance into the MAB—00 UTC 28 Aug—250-850 hPa wind shear values in NARR, WRF warm SST, and WRF cold SST runs approached 50 m s^{-1} in the near vicinity ahead of Irene's eye (**Figure 12A-C**). A radiosonde launch from Buffalo (KBUF) at the same time showed 250-850 hPa wind shear values of about 45 m s^{-1}, which matched well with NARR (45 m s^{-1}) and both WRF simulations (43 and 41 m s^{-1}); furthermore, simulated u and v wind profiles across the entire atmospheric column correlated very well with observed profiles (**Figure 12D**). Twelve hours later, wind shear values ahead of Irene in NARR and both WRF simulations approached 60 m s^{-1}, and observed wind shear at KBUF (about 43 m s^{-1}) correlated well with NARR and WRF (**Figure 12E-H**). It is important to note that these wind shear values were likely extremely detrimental to Irene's intensity, but it is clear that our WRF simulations accurately reproduced these very high values and thus wind shear was most likely not a contribution to Irene's decay that was missing in our model.

Finally, a snapshot of RH at 300 hPa and 700 hPa from WRF at 12 UTC 28 Aug shows an intrusion of dryer air into the southeast quadrant of Irene, agreeing well with a GOES water vapor image 12 minutes later (**Figure 13A-E**). This GOES image indicates dry upper levels (~300 hPa) and moist lower levels (~700 hPa) in the southern half of the storm, with moist upper and lower levels in the northern half; WRF matches well. A radiosonde launched from Wallops Island (KWAL), which was situated in the storm's southern half at this time, showed the same story, with WRF actually drying out the atmosphere more than observed between 700 and 300 hPa (**Figure 13F**). Overdrying the mid-levels would presumably result in additional decreases in storm intensity, so it is clear that any dry air intrusion was also not an neglected contribution to Irene's decay.

4. Discussion

In summary, significant ahead-of-eye SST cooling (at least 5°C and up to 11°C) occurred in the MAB during Hurricane Irene (2011). Coupled ocean-atmosphere hurricane models did not resolve this coastal ocean cooling process in their predictions, and basic satellite SST products did not capture the result of the cooling. In this paper, we address the consequences of not resolving the ahead-of-eye cooling process in modeling by quantifying the sensitivity of Irene's intensity, size, and structure to the SST cooling. The intensity sensitivity to the ahead-of-eye cooling turned out to be the largest among tested model parameters, surpassing sensitivity to the parameterization of air-sea fluxes themselves. Storm size and structure sensitivity to the ahead-of-eye cooling was comparatively low.

Furthermore, accounting for the ahead-of-eye SST cooling in our modeling through the use of a fixed cold post-storm SST that captured the cooling mitigated the high bias in model predictions. Validation of modeled heat fluxes indicated that the cold SST simulation accurately reversed the sign of latent heat flux over the MAB as observed by two NDBC buoys. This would confirm the use of post-storm SST fixed through simulation so that Irene would propagate over the colder "pre-mixed" waters, even though some slight cooling did indeed occur after eye passage. Finally, our simulations handled track, wind shear, and dry air intrusion very well, indicating that upper ocean thermal evolution was the key missing contribution to Irene's decay just prior to NJ landfall.

Simplistic 1D ocean models are incapable at resolving the 3D coastal ocean processes responsible for ahead-of-eye cooling. Rather, a 3D high resolution coastal ocean model, such as ROMS, nested within a synoptic or global-scale ocean model like HYCOM could begin to spatially and temporally resolve this evidently important process, adding significant value to TC prediction in the coastal ocean—the last hours before landfall where impacts (storm surge, wind damage, and inland flooding) are greatest and are most closely linked with changes in storm intensity. A ROMS simulation at 5km horizontal resolution over the MAB not specifically designed for TCs can begin to resolve this ahead-of-eye cooling spatially (**Figure 14**). This moderately accurate treatment of TC cooling, however, was arrived at through the combination of weak wind forcing from NAM (max winds ~10 m s^{-1} too low) and a broad initial thermocline—a right answer for the wrong reasons. Some issues with ROMS' SST cooling do remain, including insufficient cooling in the southern MAB and surface waters warming too quickly post-storm. Further improvements can be expected with: 1) even higher horizontal and vertical resolution that can resolve the sharp initial thermocline, 2) better mixing physics/turbulence closure schemes, and 3) more accurate wind forcing. Only after these improvements is it suggested to employ a coupled ocean-atmosphere modeling framework to resolve ahead-of-eye cooling.

Future work is three-fold. First, better ocean data, e.g. more coastal ocean profile time series, will be needed to better spatially validate coastal ocean models. Second, a greater number of in-depth case studies of ahead-of-eye cooling (several are listed in Glenn et al. 2015) are necessary to build a more robust assessment of the dependence of TC intensity prediction on coastal oceans, across all seasons and across all TC basins. Finally, movement towards a fully coupled atmosphere-ocean-wave system is critical. Wave breaking was not investigated in this study but may also contribute significantly to TC mixing of stratified coastal seas (Sullivan and McWilliams 2010).

Acknowledgments

Support was provided by the New Jersey Board of Public Utilities (2010RU-COOL, BP-070), the Environmental Protection Agency (EP-11-C-000085), the New Jersey Department of Environmental Protection (WM13-019-2013), the National Oceanic and Atmospheric Administration (NOAA) led Integrated Ocean Observing System through the Mid-Atlantic Regional Association Coastal Ocean Observing System (MARACOOS, NA11NOS0120038), NOAA Cooperative Institute for the North Atlantic Region (NA13OAR4830233), and Rutgers University. We would also like to thank Hyun-Sook Kim and Zhan Zhang of the HWRF team at NCEP for providing the HWRF-POM and HWRF-HYCOM data. Finally, we would like to thank John Wilkin at Rutgers University for his discussion and suggestions regarding the ocean modeling and upper air validation, the research associates of the Rutgers Ocean Modeling group for their help with ROMS, and Rich Dunk for his helpful meteorological discussions and ideas.

References

Avila, L. A., and J. Cangialosi, 2012: Tropical Cyclone Report: Hurricane Irene (AL092011). *Natl. Hurric. Cent. Trop. Cyclone Rep.*, 45. http://www.nhc.noaa.gov/data/tcr/AL092011_Irene.pdf.

Bender, M. a., I. Ginis, and Y. Kurihara, 1993: Numerical simulations of tropical cyclone-ocean interaction with a high-resolution coupled model. *J. Geophys. Res.*, **98**, 23245, doi:10.1029/93JD02370.

Cangialosi, J. P., and J. L. Franklin, 2013: *2012 National Hurricane Center Forecast Verification Report*. 1-79 pp.

Chang, S. W., and R. A. Anthes, 1979: The Mutual Response of the Tropical Cyclone and the Ocean. *J. Phys. Oceanogr.*, **9**, 128–135.

D'Asaro, E. a., 2003: The Ocean Boundary Layer below Hurricane Dennis. *J. Phys. Oceanogr.*, **33**, 561–579, doi:10.1175/1520-0485(2003)033<0561:TOBLBH>2.0.CO;2.

Davis, C., and Coauthors, 2008: Prediction of Landfalling Hurricanes with the Advanced Hurricane WRF Model. *Mon. Weather Rev.*, **136**, 1990–2005, doi:10.1175/2007MWR2085.1.

Emanuel, K., 2003: Tropical Cyclones. *Annu. Rev. Earth Planet. Sci.*, **31**, 75–104, doi:10.1146/annurev.earth.31.100901.141259. http://www.annualreviews.org/doi/abs/10.1146/annurev.earth.31.100901.141259 (Accessed January 29, 2014).

——, C. DesAutels, C. Holloway, and R. Korty, 2004: Environmental Control of Tropical Cyclone Intensity. *J. Atmos. Sci.*, **61**, 843–858, doi:10.1175/1520-0469. http://dx.doi.org/10.1175/1520-0469(2004)061<0843:ECOTCI>2.0.CO.

Emanuel, K. a., 1999: Thermodynamic control of hurricane intensity. *Nature*, **401**, 665–669, doi:10.1038/44326.

Fairall, C. W., E. F. Bradley, D. P. Rogers, J. B. Edson, and G. S. Young, 1996: Bulk parameterization of air-sea fluxes for Tropical Ocean-Global Atmosphere Coupled-Ocean Atmosphere Response Experiment. *J. Geophys. Res.*, **101**, 3747, doi:10.1029/95JC03205.

Fisher, E. L., 1958: Hurricanes and the Sea-Surface Temperature Field. *J. Meteorol.*, **15**, 328–333, doi:10.1175/1520-0469(1958)015<0328:HATSST>2.0.CO;2.

Fuglister, F. C., and L. V. Worthington, 1951: Some Results of a Multiple Ship Survey of the Gulf Stream. *Tellus A*, **3**, doi:10.3402/tellusa.v3i1.8614.

Glenn, S., C. Jones, M. Twardowski, L. Bowers, J. Kerfoot, J. Kohut, D. Webb, and O. Schofield, 2008: Glider observations of sediment resuspension in a Middle Atlantic Bight fall transition storm. *Limnol. Oceanogr.*, **53**, 2180–2196, doi:10.4319/lo.2008.53.5_part_2.2180.

Glenn, S. M., O. Schofield, T. N. Miles, G. N. Seroka, Y. Xu, H. J. Roarty, R. K. Forney, and J. T. Kohut, 2015: Ahead-of-Eye Cooling of a Stratified Coastal Ocean Reduces Tropical Cyclone Intensity. *Nat. Commun. Submitt.*,.

Green, B. W., and F. Zhang, 2013: Impacts of Air–Sea Flux Parameterizations on the Intensity and Structure of Tropical Cyclones. *Mon. Wea. Rev.*, **141**, 2308–2324, doi:10.1175/MWR-D-12-00274.1. http://journals.ametsoc.org/doi/abs/10.1175/MWR-D-12-00274.1.

Haidvogel, D. B., and Coauthors, 2008: Ocean forecasting in terrain-following coordinates: Formulation and skill assessment of the Regional Ocean Modeling System. *J. Comput. Phys.*, **227**, 3595–3624, doi:10.1016/j.jcp.2007.06.016.

Jacob, S. D., and L. K. Shay, 2003: The Role of Oceanic Mesoscale Features on the Tropical Cyclone–Induced Mixed Layer Response: A Case Study. *J. Phys. Oceanogr.*, **33**, 649–676, doi:10.1175/1520-0485(2003)33<649:TROOMF>2.0.CO;2.

Jaimes, B., and L. K. Shay, 2009: Mixed Layer Cooling in Mesoscale Oceanic Eddies during Hurricanes Katrina and Rita. *Mon. Weather Rev.*, **137**, 4188–4207, doi:10.1175/2009MWR2849.1.

Khain, A. P., and I. Ginis, 1991: The mutual response of a moving tropical cyclone and the ocean. *Contrib. to Atmos. Phys.*, **64**, 125–141.

Kim, H. S., C. Lozano, V. Tallapragada, D. Iredell, D. Sheinin, H. L. Tolman, V. M. Gerald, and J. Sims, 2014: Performance of ocean simulations in the coupled HWRF-HYCOM model. *J. Atmos. Ocean. Technol.*, **31**, 545–559, doi:10.1175/JTECH-D-13-00013.1.

Landsea, C. W., and J. L. Franklin, 2013: Atlantic Hurricane Database Uncertainty and Presentation of a New Database Format. *Mon. Weather Rev.*, **141**, 3576–3592, doi:10.1175/MWR-D-12-00254.1. http://journals.ametsoc.org/doi/abs/10.1175/MWR-D-12-00254.1.

Leipper, D. F., 1967: Observed Ocean Conditions and Hurricane Hilda, 1964. *J. Atmos. Sci.*, **24**, 182–186, doi:10.1175/1520-0469(1967)024<0182:OOCAHH>2.0.CO;2.

Lynn, B. H., and Coauthors, 2015: The sensitivity of Hurricane Irene to aerosols and ocean coupling: simulations with WRF spectral bin microphysics. *J. Atmos. Sci.*, 150413133444005, doi:10.1175/JAS-D-14-0150.1. http://journals.ametsoc.org/doi/abs/10.1175/JAS-D-14-0150.1.

Marks, F. D., and Coauthors, 1998: Landfalling Tropical Cyclones:Forecast Problems and Associated Research Opportunitis. *Bull.*, **79**, 305–321.

Miles, T., S. Glenn, and O. Schofield, 2013: Temporal and spatial variability in fall storm induced sediment resuspension on the Mid-Atlantic Bight. *Cont. Shelf Res.*, **63**.

Miles, T. N., G. N. Seroka, J. T. Kohut, O. Schofield, and S. M. Glenn, 2015: Glider observations and modeling of sediment transport in Hurricane Sandy. *J. Geophys. Res. Ocean.*, **120**, 1771–1791, doi:10.1002/2014JC010474.Received.

Pollard, R. T., P. B. Rhines, and R. O. Thompson, 1972: The deepening of the wind-mixed layer. *Geophys. Astrophys. Fluid Dyn.*, **4**, 381–404.

Reynolds, R. W., and D. B. Chelton, 2010: Comparisons of daily Sea surface temperature analyses for 2007-08. *J. Clim.*, **23**, 3545–3562, doi:10.1175/2010JCLI3294.1.

Ruiz, S., L. Renault, B. Garau, and J. Tintoré, 2012: Underwater glider observations and modeling of an abrupt mixing event in the upper ocean. *Geophys. Res. Lett.*, **39**, n/a – n/a, doi:10.1029/2011GL050078.

Sampson, C. R., and A. J. Schrader, 2000: The Automated Tropical Cyclone Forecasting System (version 3.2). *Bull. Am. Meteorol. Soc.*, **81**, 1231–1240, doi:10.1175/1520-0477(2000)081<1231:TATCFS>2.3.CO;2.

Schade, L. R., and K. a. Emanuel, 1999: The Ocean's Effect on the Intensity of Tropical Cyclones: Results from a Simple Coupled Atmosphere–Ocean Model. *J. Atmos. Sci.*, **56**, 642–651, doi:10.1175/1520-0469(1999)056<0642:TOSEOT>2.0.CO;2.

Schofield, O., and Coauthors, 2007: Slocum Gliders: Robust and ready. *J. F. Robot.*, **24**, 473–485, doi:10.1002/rob.20200.

Skamarock, W., J. Klemp, and J. Dudhia, 2005: A description of the advanced research WRF version 2. *NCAR Tech. NOTE*, **468**. http://oai.dtic.mil/oai/oai?verb=getRecord&metadataPrefix=html&identifier=ADA487419 (Accessed April 11, 2014).

Suda, K., 1943: *Ocean Science*. Kokin-Shoin, Tokyo,.

Sullivan, P. P., and J. C. McWilliams, 2010: Dynamics of Winds and Currents Coupled to Surface Waves. *Annu. Rev. Fluid Mech.*, **42**, 19–42, doi:10.1146/annurev-fluid-121108-145541.

Sutyrin, G. G., and E. A. Agrenich, 1979: Interaction of the boundary layers of the ocean and atmosphere in a tropical cyclone. *Meteor. Gidrol.*, **2**, 45–56.

——, and A. P. Khain, 1984: The Influence of the Ocean-Atmosphere Interaction on the Intensity of Moving Tropical Cyclones. *Izv. Akad. Nauk SSSR Fiz. Atmos. I Okeana*, 787–794.

Tallapragada, V., S. Gopalakrishnan, Q. Liu, and T. Marchok, 2011: Hurricane Weather Research and Forecasting (HWRF) model: 2011 scientific documentation. *Dev. Testbed Cent.*, 1–96. http://www.dtcenter.org/HurrWRF/users/docs/scientific_documents/HWRFScientificDocumentation_August2011.pdf.

Torn, R. D., and C. Snyder, 2012: Uncertainty of Tropical Cyclone Best-Track Information. *Weather Forecast.*, **27**, 715–729, doi:10.1175/WAF-D-11-00085.1.

Wilkin, J. L., and E. J. Hunter, 2013: An assessment of the skill of real-time models of Mid-Atlantic Bight continental shelf circulation. *J. Geophys. Res. Ocean.*, **118**, 2919–2933, doi:10.1002/jgrc.20223.

Table 1. List of model sensitivities, grouped by type. Name of sensitivity is on left, details of sensitivity with WRF namelist option on right.

Sensitivity	**WRF Namelist Option**
A. Model Configuration	
1. Horizontal resolution (*dx*)	3 km vs. 6 km
2. Vertical resolution (*e_vert, eta_levels*)	51 vs. 35 vertical levels
3. Adaptive time step (*use_adaptive_time_step*)	on vs. off
4. Boundary conditions (update frequency, *interval_seconds*)	3 vs. 6 hours
5. Digital Filter Initialization (DFI, *dfi_opt*)	on vs. off
B. Atmospheric/Model Physics	
6. Microphysics (*mp_physics*)	6 (WRF Single-Moment 6-class) vs.
	16 (WRF Double-Moment 6-class)
7-8. Planetary boundary layer scheme (*bl_pbl_physics*)	5 (Mellor-Yamada Nakanishi and Niino Level 2.5) vs. 7 (ACM2) vs.
	1 (Yonsei University)
9. Cumulus parameterization (*cu_physics*)	1 (Kain-Fritsch, *cudt*=0, *cugd_avedx*=1) vs. 0 (off)
10. SST skin (*sst_skin*)	on vs. off
11-13. Longwave radiation (*ra_lw_physics*)	1 (RRTM) vs. 5 (New Goddard) vs.
	99 (GFDL) vs. 4 (RRTMG)
14-16. Shortwave radiation (*ra_sw_physics*)	1 (Dudhia) vs. 5 (New Goddard) vs.
	99 (GFDL) vs. 4 (RRTMG)
17-18. Latent heat flux <0 over water (in module_sf_sfclay)	on vs. off (warm SST)
	on vs. off (cold SST)
19. Land surface physics (*sf_surface_physics*)	1 (5-layer thermal diffusion) vs.
	2 (Noah)
C. Advanced Hurricane WRF (AHW) Options	
20-21. Air-sea flux parameterizations (*isftcflx*)	1 vs. 0 (warm SST)
	1 vs. 0 (cold SST)
22-23. 1D Ocean Mixed Layer Model (*omlcall*)	on vs. off
	on w/ HyCOM vs. off
D. Sea Surface Temperature	
24-26. SST	cold vs. warm (isftcflx=2)
	cold vs. warm (isftcflx=1)
	cold vs. warm (isftcflx=0)

Table 2. Radius of maximum 10m winds in nautical miles. Warm SST and cold SST simulations compared to b-deck data from the ATCF system database.

Radius of Maximum Wind (nmi)			
Time	Bdeck	Warm SST	Cold SST
06UTC 27 Aug	60	58	58
12UTC 27 Aug	45	43	43
18UTC 27 Aug	45	55	56
00UTC 28 Aug	45	39	46
06UTC 28 Aug	100	40	40
12UTC 28 Aug	100	115	151

Table 3. Track error in kilometers as compared to NHC best track data, for the warm and cold SST simulations.

Track error (km)		
Time	**Warm SST**	**Cold SST**
06UTC 27 Aug	12	12
12UTC 27 Aug	23	23
18UTC 27 Aug	13	11
00UTC 28 Aug	16	10
06UTC 28 Aug	5	14
09:35UTC 28 Aug	8	28
12UTC 28 Aug	25	44
13UTC 28 Aug	26	48

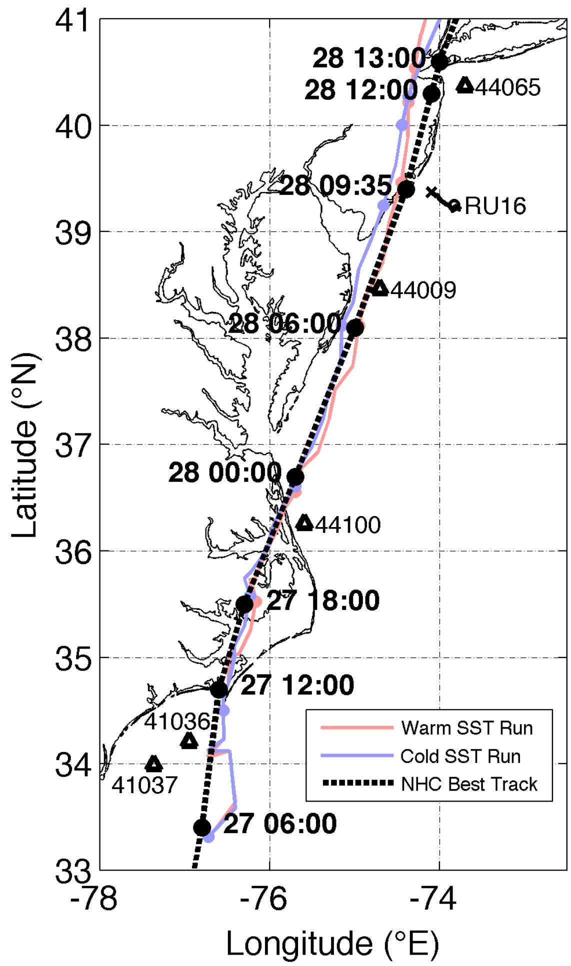

Figure 1. NHC best track data for Hurricane Irene, in dashed black. Warm (red) and cold (blue) SST simulations are also plotted. NDBC buoy locations are shown with black triangles, and RU16 glider track depicted in solid black, with beginning of the storm period denoted by an 'x' and end denoted by a circle.

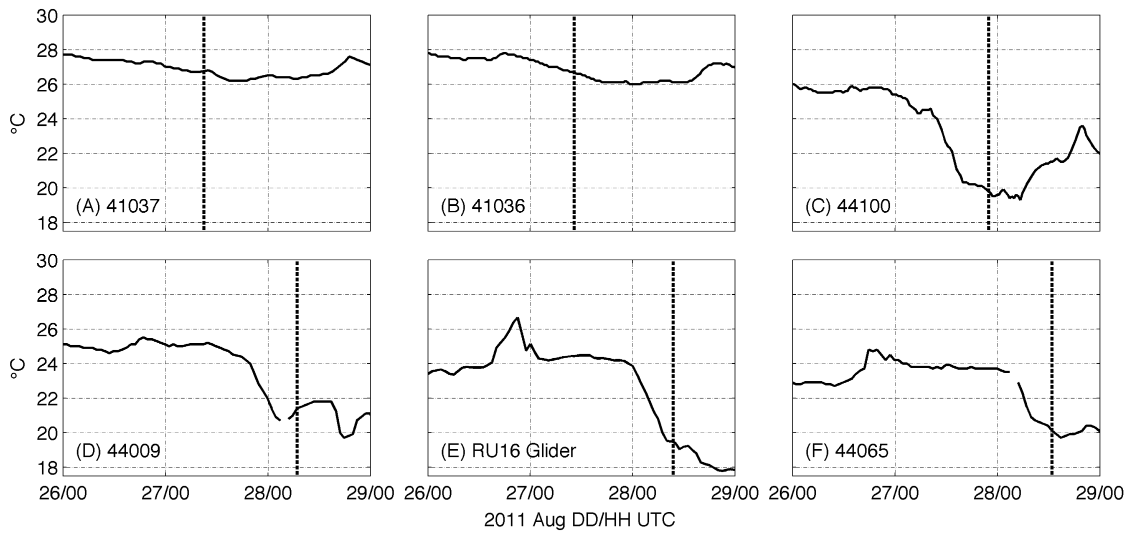

Figure 2. NDBC buoy and glider near surface water temperature (°C) time series. South Atlantic Bight buoys from south to north are 41037 and 41036, and Mid Atlantic Bight buoys and RU16 glider from south to north are 44100, 44009, RU16 glider, and 44065. Timing of Irene's eye passage by the buoy or glider denoted with vertical dashed line.

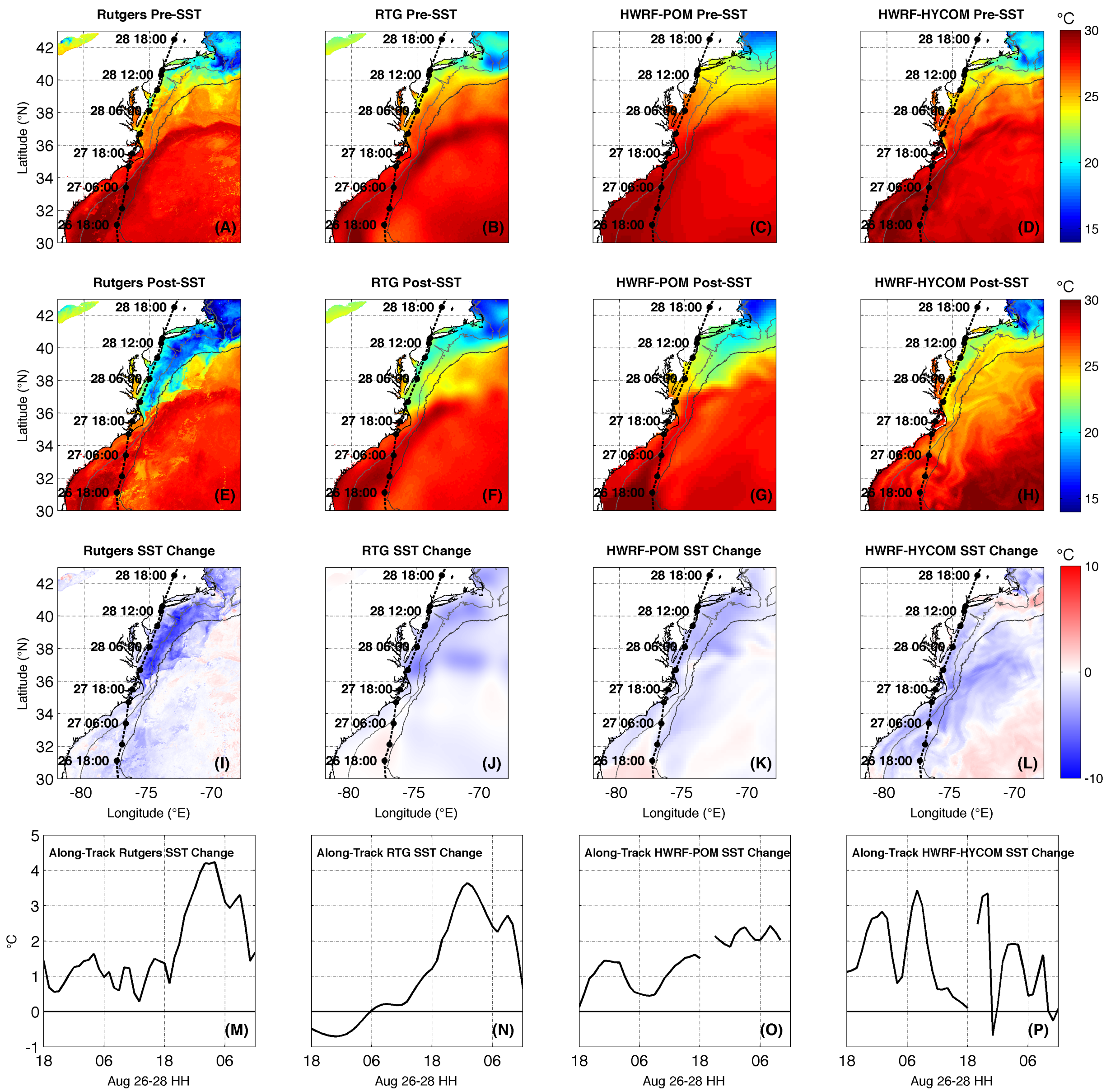

Figure 3. SST plots before Irene (A-D) at 00UTC 26 Aug 2011, after Irene (E-H) at 00UTC 31 Aug 2011, difference between before and after (I-L), and along-track SST change (M-P). First column is the new "Rutgers" SST composite, which combines AVHRR and NASA SPoRT SST data. Second column is Real-Time Global High Resolution (RTG HR) SST product from NOAA. Third column is the operational HWRF-POM from 2011, simulation initialized at 00UTC 26 Aug 2011. Fourth column is the experimental HWRF-HYCOM from 2011, simulation initialized at 00UTC 26 Aug 2011.

Group	Name	Options
Model Setup	Horizontal resolution	3km vs. 6km
	Vertical resolution	51 vs. 35 levels
	Adaptive time step	on vs. off
	B.C. (Frequency)	3 hrs vs. 6 hrs
	Digital Filter Initialization (DFI)	on vs. off
Atmospheric/ Model Physics	Microphysics	6 vs. 16
	PBL scheme	5 vs. 1
		7 vs. 1
	Cumulus parameterization	1 vs. 0
	SST skin	on vs. off
	Longwave radiation physics	1 vs. 4
		5 vs. 4
		99 vs. 4
	Shortwave radiation physics	1 vs. 4
		5 vs. 4
		99 vs. 4
	Latent heat flux <0 over water	on vs. off (warm SST)
		on vs. off (cold SST)
	Land surface physics	1 vs. 2
Advanced Hurricane WRF	Air-sea flux parameterizations	1 vs. 0 (warm SST)
		1 vs. 0 (cold SST)
	1D Ocean Mixed Layer Model	on vs. off
		on w/ HyCOM vs. off
Sea Surface Temperature	SST	Warm vs. Cold (isftcflx=2)
		Warm vs. Cold (isftcflx=1)
		Warm vs. Cold (isftcflx=0)

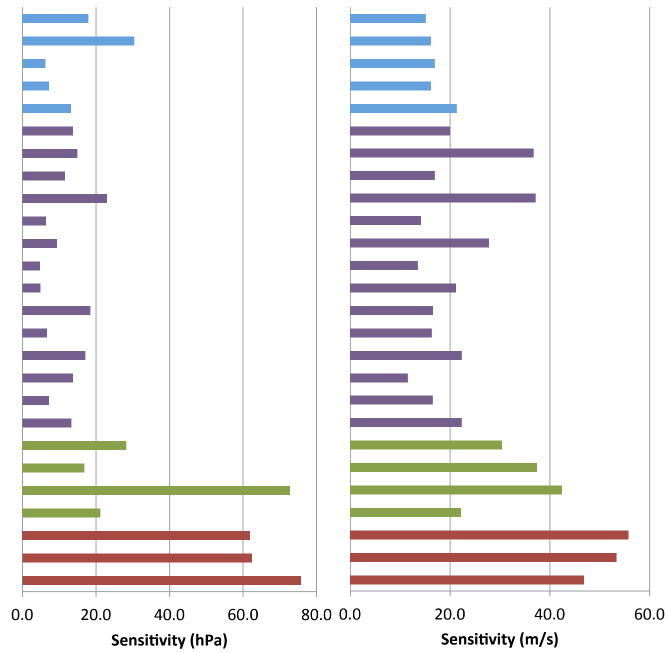

Figure 4. Cumulative model sensitivity results, from 23UTC 27 Aug (start of Irene's presence over MAB) to 18UTC 28 Aug (end of simulation). Group, name, and WRF namelist options on left with control run namelist option listed last for each sensitivity. Minimum sea level pressure (hPa) sensitivity on left and maximum sustained 10m wind (m/s) sensitivity on right.

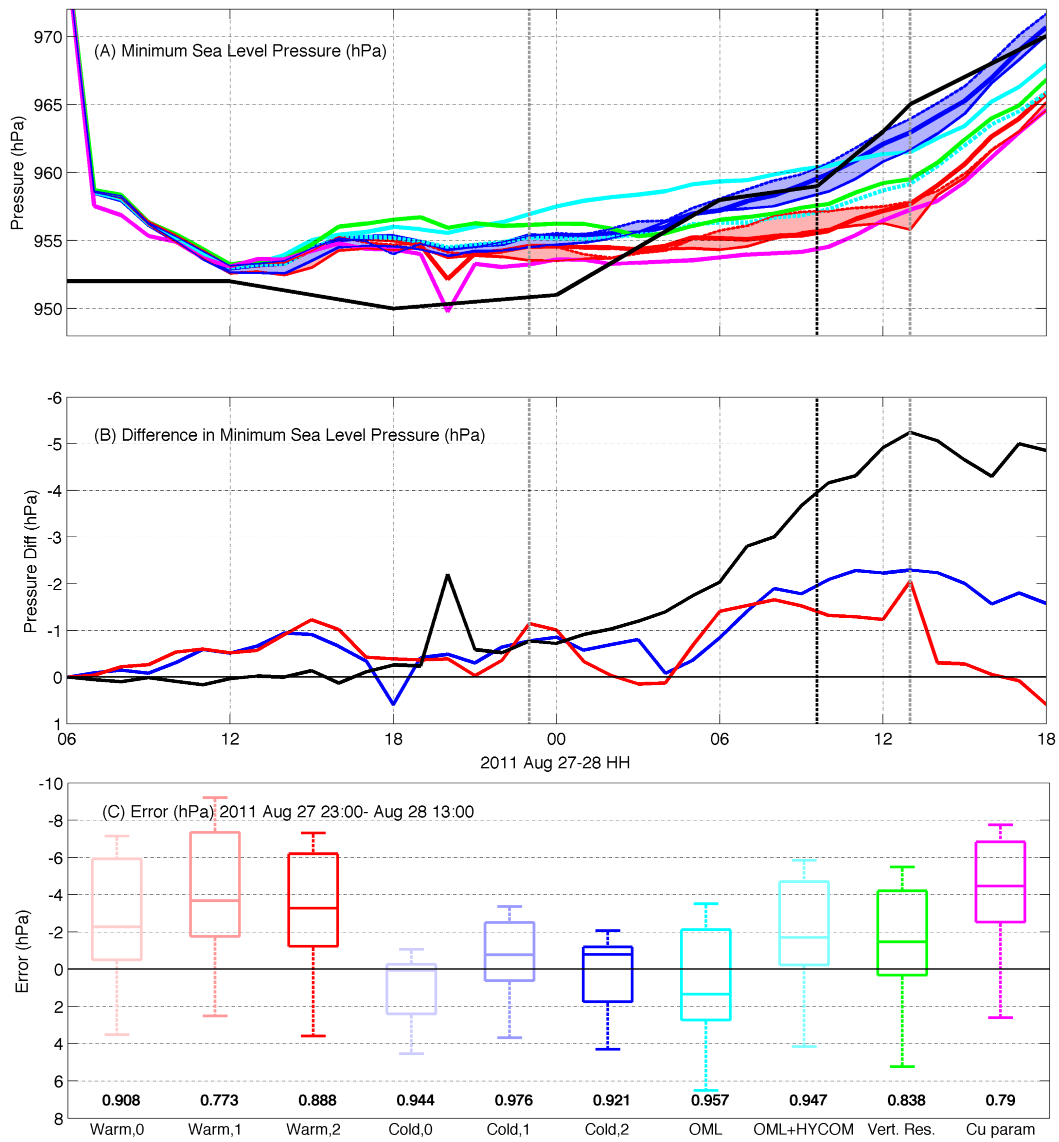

Figure 5. Minimum sea level pressure (hPa) time series (A), with NHC best track in black, warm SST with isftcflx=0 in thin dashed red, warm SST with isftcflx=1 in thin red, warm SST with isftcflx=2 in thick red, the three cold SST runs the same as warm SST but in blue lines, 1D ocean mixed layer model with initial mixed layer depth at 10m and slope of thermocline at 1.6°C/m everywhere in solid cyan, 1D ocean mixed layer model with initial mixed layer depth from HYCOM and slope of thermocline at 1.6°C/m everywhere in dashed cyan, vertical resolution of 3km in green, and cumulus paramterization turned on in magenta. Vertical dashed gray lines depict start and end of Irene's presence over the MAB (23UTC 27 Aug to 13UTC 28 Aug), with vertical dashed black line depicting Irene's landfall in NJ. Difference in central pressure (B) between warm and cold SST runs with isftcflx=2 in black, between isftcflx=0 and 1 for warm SST in red, and between isftcflx=0 and 1 for cold SST in blue. Finally, box and whisker plots of errors vs. NHC best track data (C) during Irene's MAB presence, with r-squared values in bold.

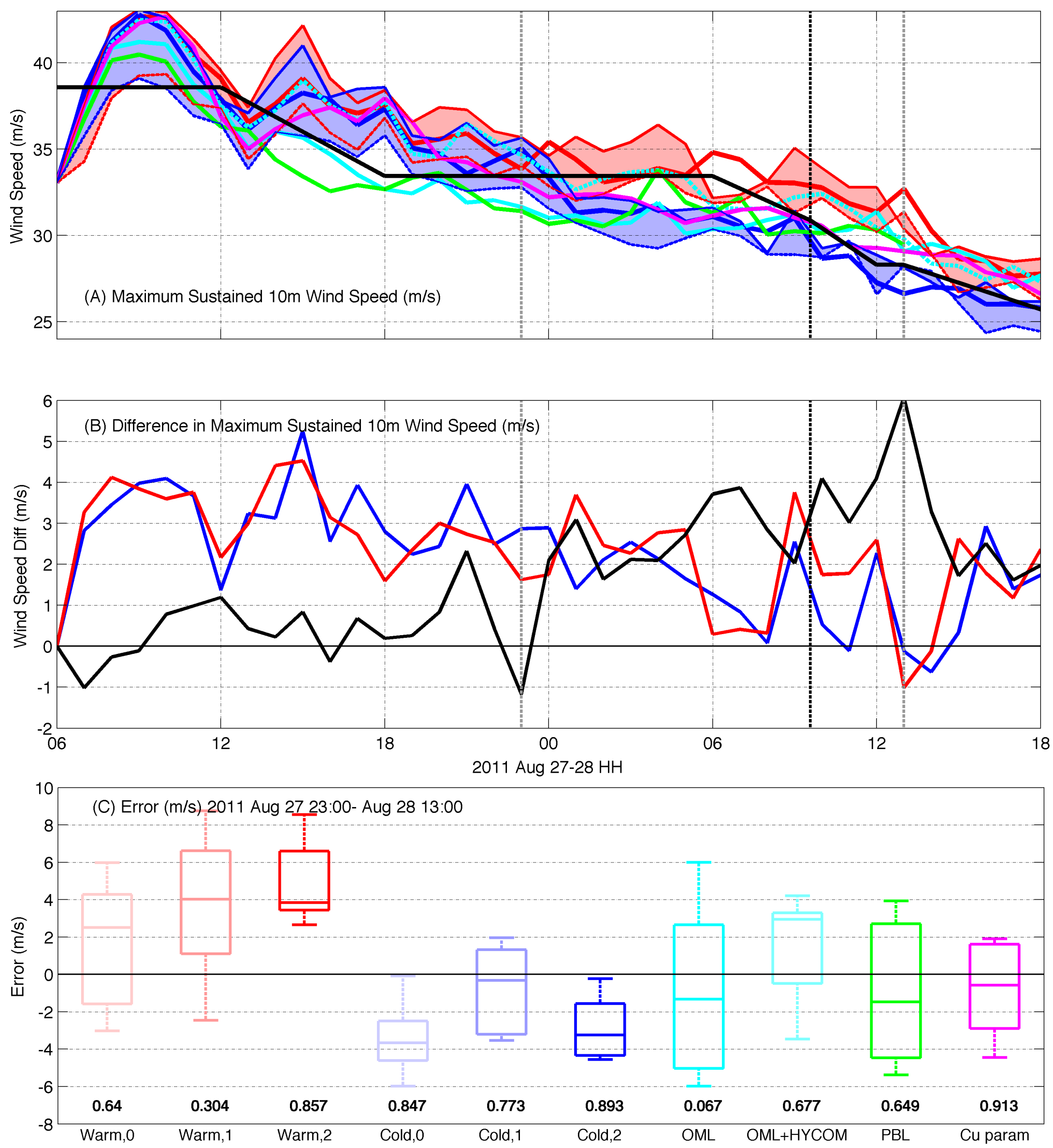

Figure 6. The same as Figure 5, but for maximum sustained 10m winds (m/s).

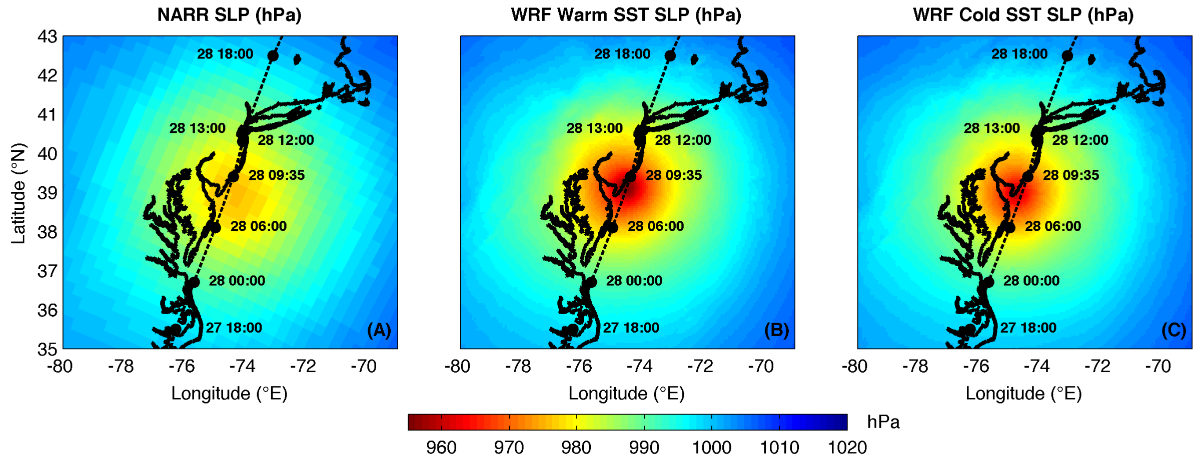

Figure 7. Spatial plot of SLP (hPa) at 09UTC 28 Aug just prior to NJ landfall, with Irene's NHC best track in dashed black, NARR (A), WRF warm SST (B), and WRF cold SST (C).

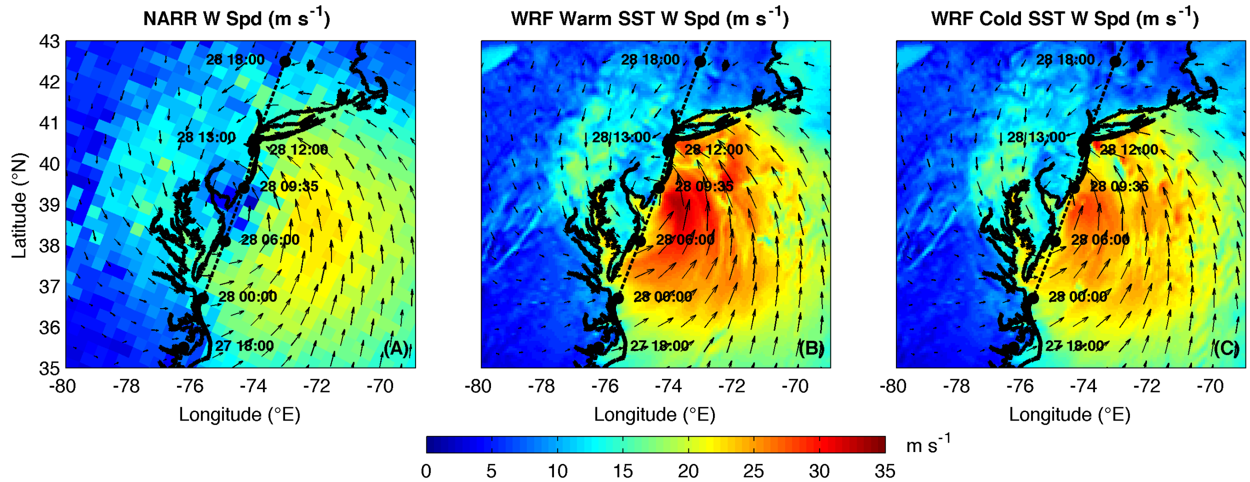

Figure 8. The same as Figure 7 but for 10m winds (m/s).

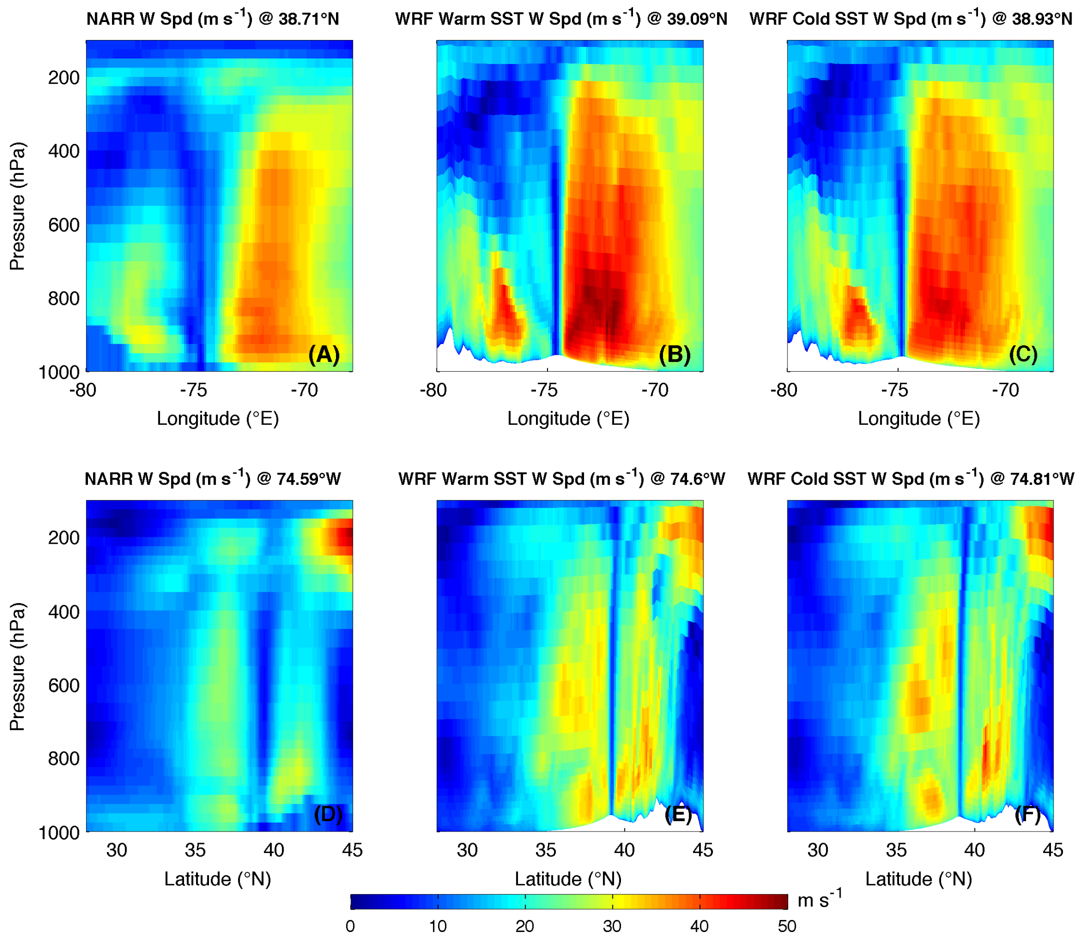

Figure 9. Vertical cross sections of wind speed through Irene's eye at 09UTC 28 Aug, just prior to NJ landfall. Top row (A-C) are west-to-east cross sections, while bottom row (D-F) are south-to-north cross sections. For each, latitude and longitude of eye is determined by locating the minimum SLP for NARR (A, D), WRF warm SST (B, E) and WRF cold SST (C, F).

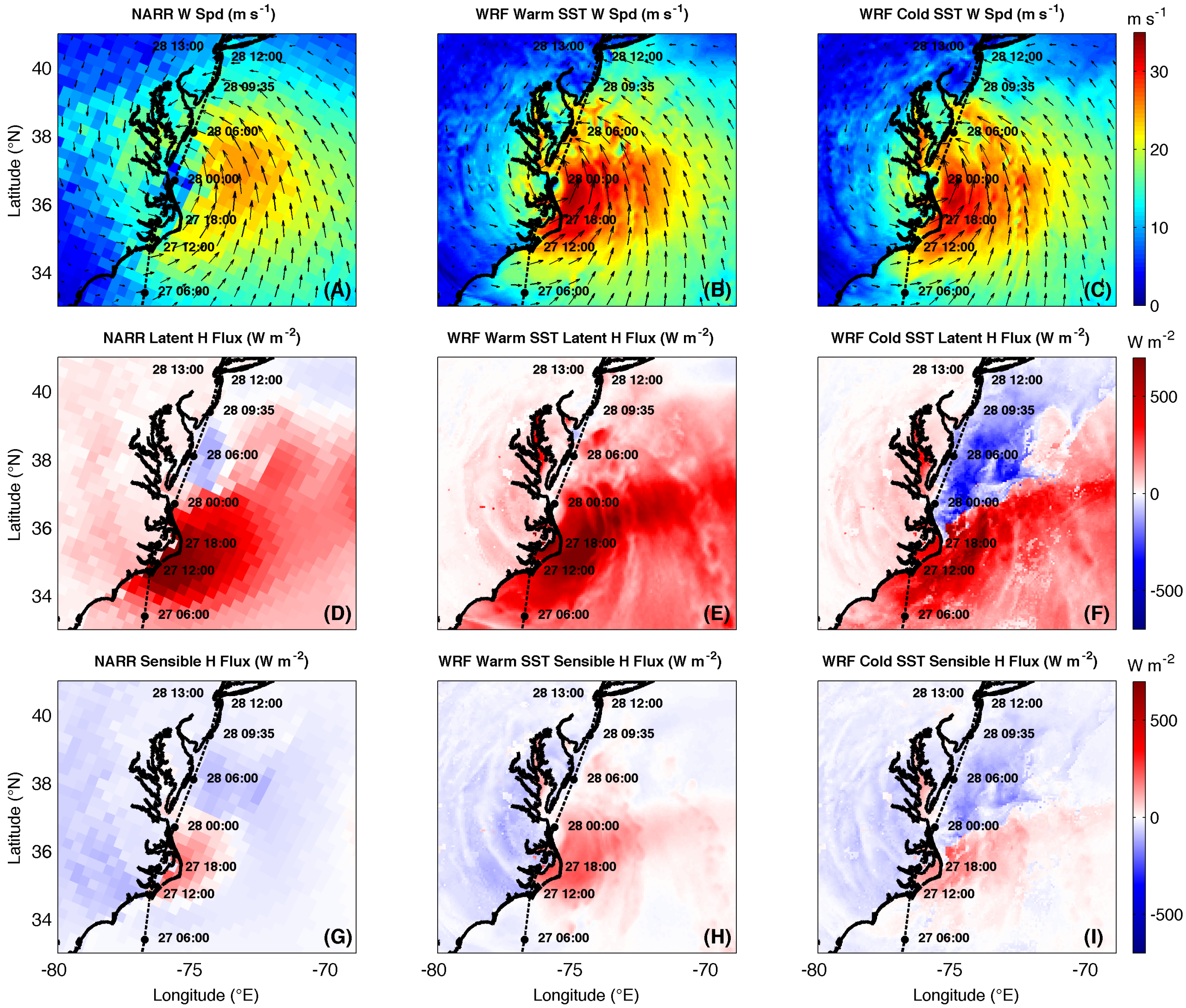

Figure 10. Spatial plots of 10m winds (m/s, A-C), latent heat flux at the surface (W m^{-2}, D-F), and sensible heat flux at the surface (W m^{-2}, G-I), at 00UTC 28 Aug. Fluxes are positive directed from water or land to atmosphere. NARR is first column (A, D, G) with fluxes shown as 3-hr averages ending at 00UTC 28 Aug, WRF warm SST is second column (B, E, H) with fluxes shown as instantaneous, and WRF cold SST (with negative latent heat flux allowed) is third column (C, F, I) with fluxes also shown as instantaneous.

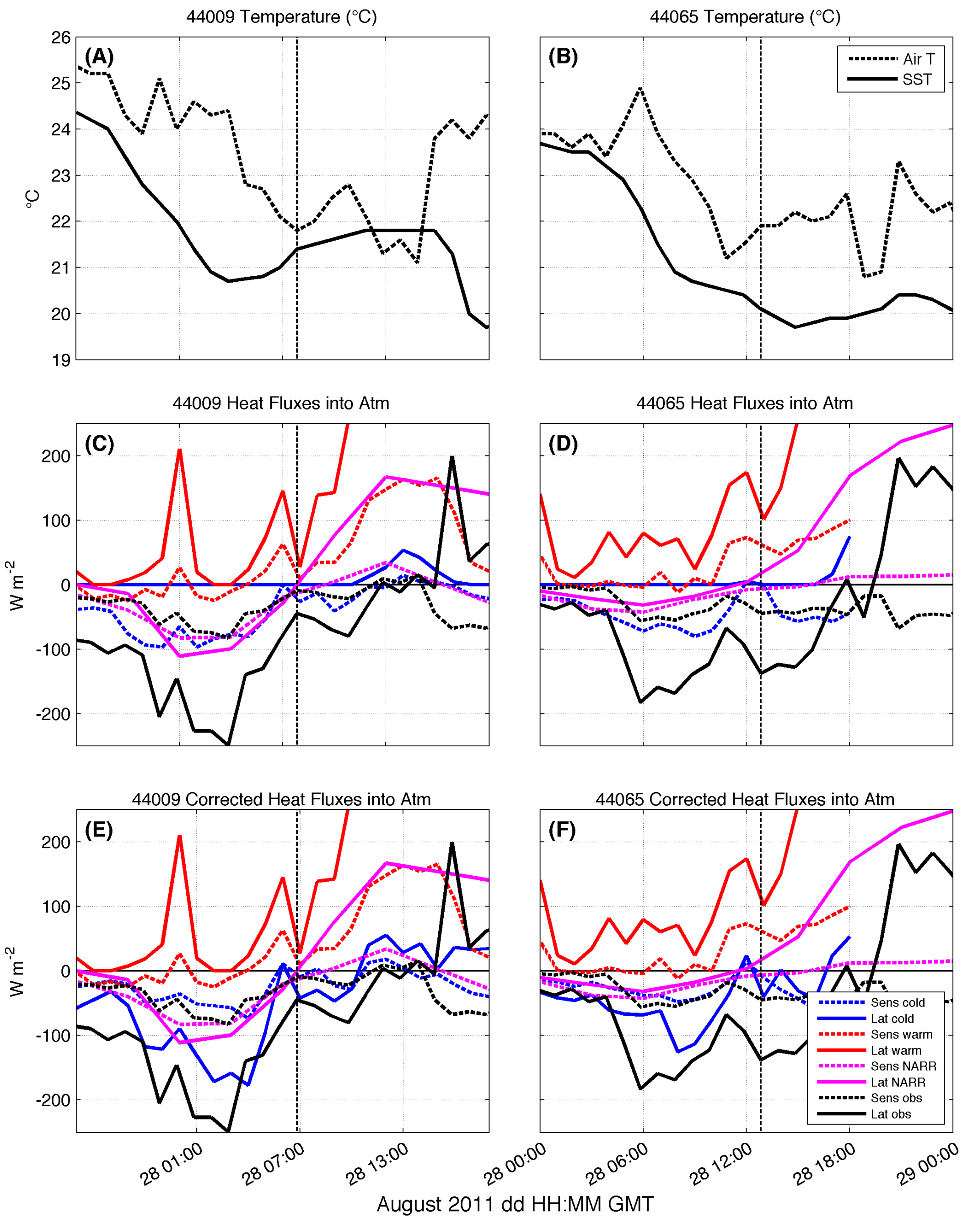

Figure 11. Time series of air temperature (°C, dashed) and near surface water temperature (°C, solid) at buoy 44009 (A) and 44065 (B), with vertical dashed line indicating timing of eye passage by that buoy (note the time axes are different for each buoy). Sensible (dashed) and latent (solid) heat fluxes (W m^{-2}) shown for the same buoys in (C) and (D) for observed (black), NARR (magenta, 3-hr flux averages), warm SST (red), and cold SST (blue). Fluxes are positive from ocean to atmosphere. Finally, the last row (E and F) show the same fluxes for observed and NARR as in C and F but WRF fluxes are corrected to allow for negative latent heat flux.

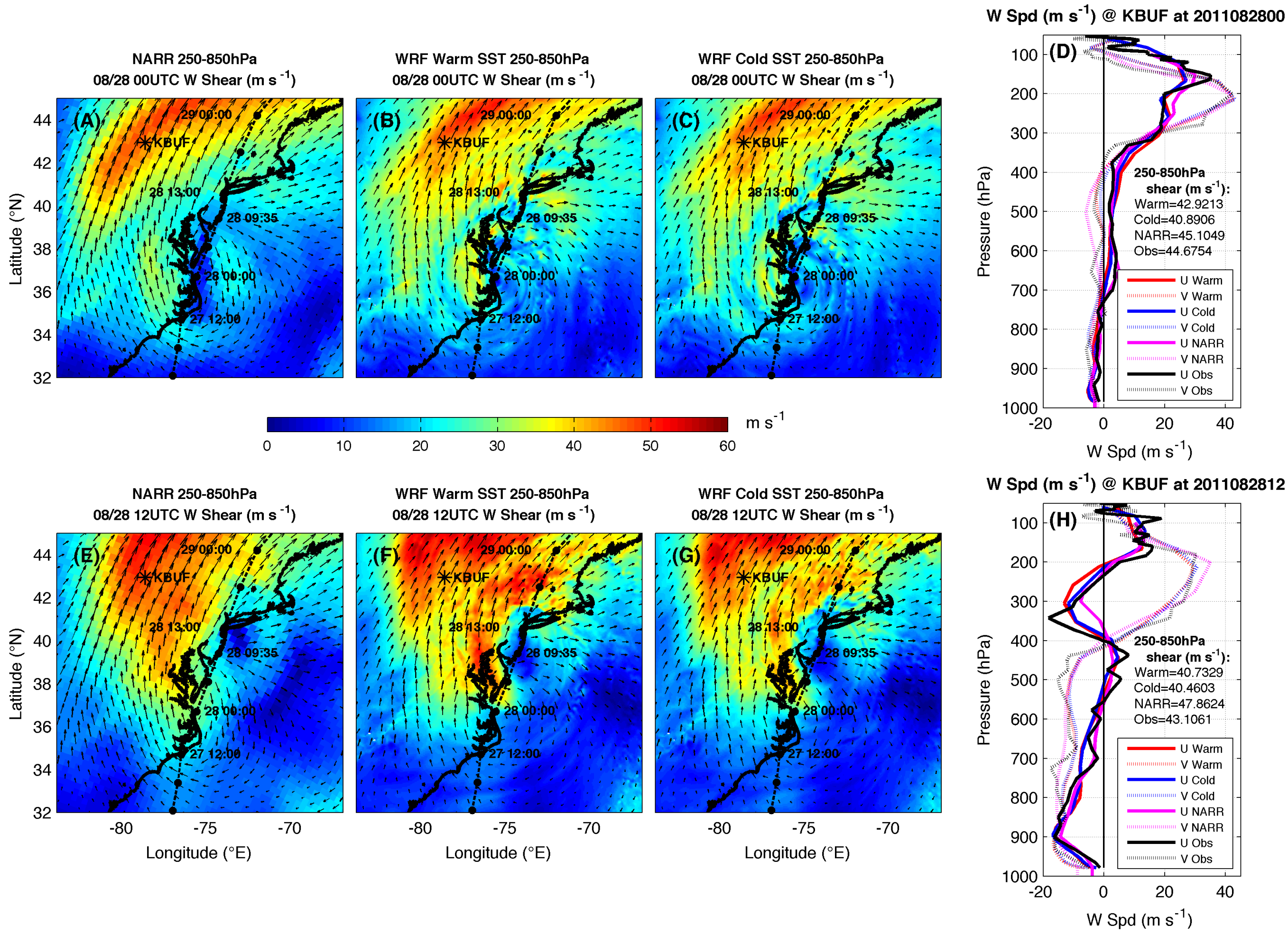

Figure 12. Wind shear validation, with top row (A-D) at 00UTC 28 Aug and bottom row (E-H) at 12UTC 28 Aug. Spatial plots are 250-850 hPa wind shear (m/s), with NARR in first column (A, E), WRF warm SST in second column (B, F) and WRF cold SST in third column (C, G). KBUF indicated by a labeled star on maps and upper air radiosonde data at KBUF plotted in fourth column (D, H), with solid lines for u-winds and dashed lines for v-winds, and observed in black, NARR in magenta, WRF cold SST in blue, and WRF warm SST in red. 250-850 hPa wind shear values (m/s) are labeled for observed, NARR, and WRF simulations on graph.

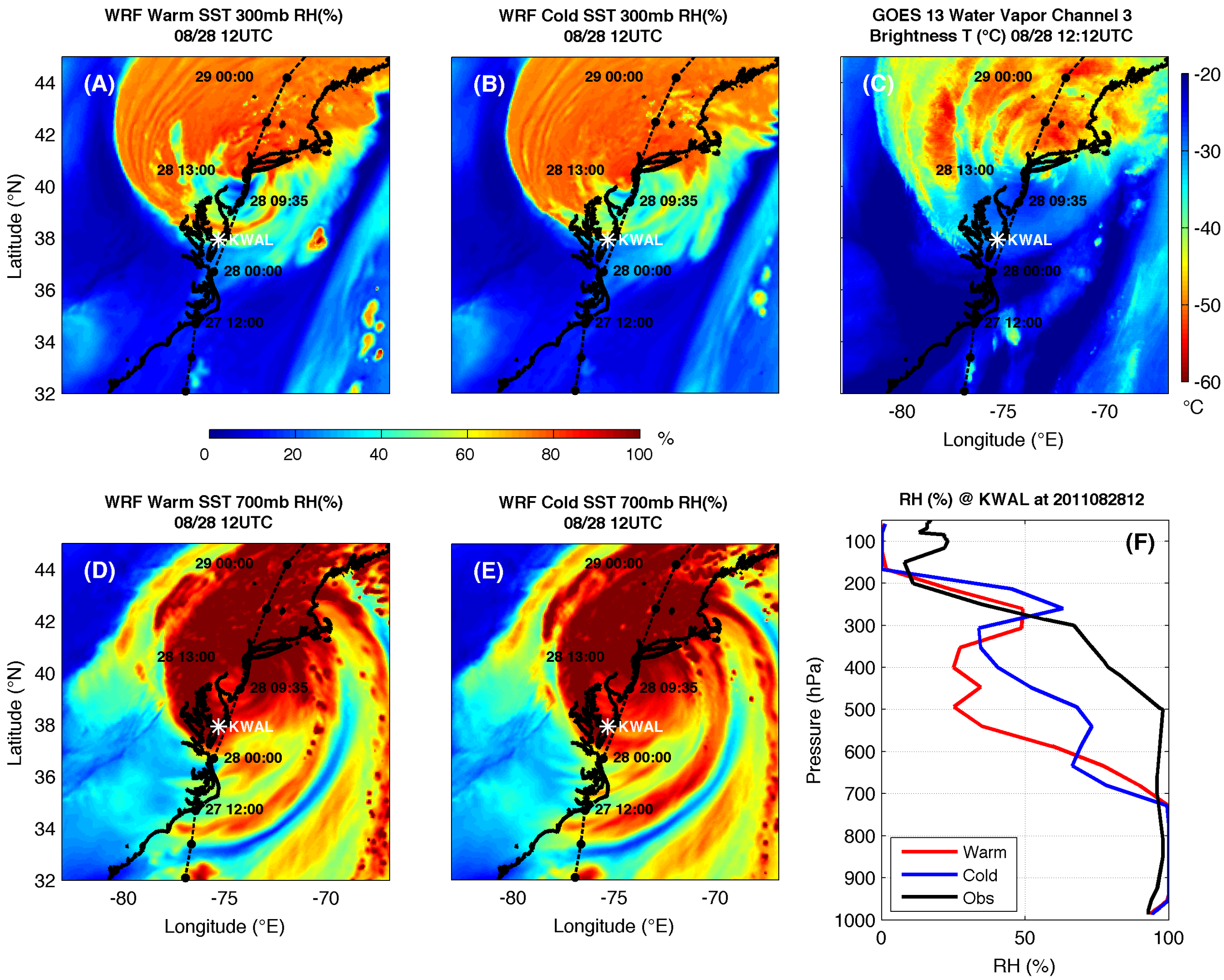

Figure 13. Dry air intrusion validation (relative humidity, RH, %) at 12UTC 28 Aug, with WRF warm SST in first column (A, D); cold SST in second column (B, E); and GOES 13 water vapor channel 3 brightness temperature (°C) at 12:12UTC 28 Aug (C) and upper air radiosonde relative humidity (%) at KWAL with observed in black, WRF warm SST in red, and WRF cold SST in blue (F) in third column. Top row (A, B) are WRF RH (%) at 300 mb for upper atmosphere, and bottom row (D, E) are WRF RH (%) at 700 mb for mid- to lower-atmosphere.

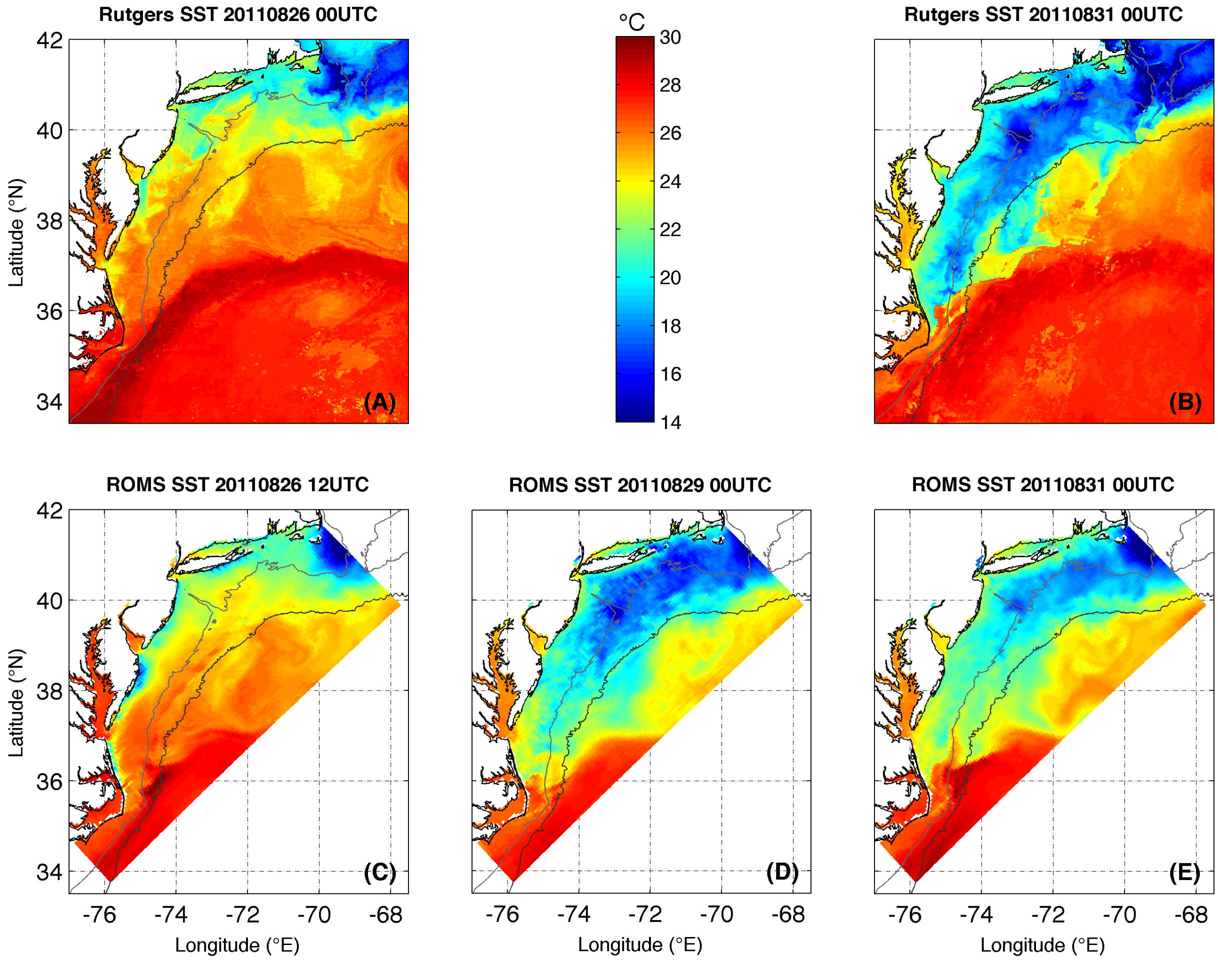

Figure 14. SST from the new "Rutgers" SST composite in top row from before Irene at 00UTC 26 Aug (A) to after Irene at 00UTC 31 Aug (B). Bottom row is water temperature of top layer from a ROMS ESPreSSO simulation, with before Irene at 12UTC 26 Aug (simulation initialization) on left (C), just after Irene at 00UTC 29 Aug in middle (D), and after Irene at 00UTC 31 Aug on right (E).